Available online at www.sciencedirect.com
SCIENCE DIRECT®
Journal of Sound and Vibration 283 (2005) 369–400
JOURNAL OF SOUND AND VIBRATION
www.elsevier.com/locate/jsvi

Noise generation mechanisms in claw pole alternators

W. Eversman[a,*], S. Burns[a], S. Pekarek[b], Hua Bai[b], J. Tichenor[b]

[a]*Department of Mechanical and Aerospace Engineering and Engineering Mechanics, University of Missouri-Rolla, 202 Mechanical Engineering Building, 1870 Miner circle, Rolla, MO 65401, USA*
[b]*Electrical and Computer Engineering, University of Missouri-Rolla, 202 Mechanical Engineering Building, 1870 Miner circle, Rolla, MO 65401, USA*

Received 20 May 2002; accepted 19 April 2004
Available online 5 November 2004

Abstract

Noise of claw pole alternators, generated electromagnetically and structurally radiated, has been the subject of an extensive research program. The goal has been to identify and reduce noise radiation mechanisms in claw pole (Lundell) alternators used in automotive applications. Two approaches have been followed. In the first, electromagnetic sources of noise have been investigated by lumped parameter and magnetically equivalent circuit modeling and simulation, and by related experimentation. This is the subject of separate papers. The second, concurrent study reported here has investigated machine and mount responses to an electromagnetically generated torque ripple. Modeling and experimentation has led to the conclusion that there exists a high correlation between electromagnetic sources, torque ripple, and radiated noise. Experimentation also has led to the conclusion that noise characteristics of a given machine are substantially altered by modification of the mounting configuration. The work reported here involves modeling, simulation, and experiment to isolate machine dynamic characteristics and mounting geometries which contribute to strong coupling between torque ripple and machine/mount dynamic response. A low-order model of the alternator which includes shaft flexibility, gyroscopic effects, shaft bearing asymmetry, mounting lug geometry, and mounting structure dynamics has been created. The model provides a rapid simulation of dynamic response in the form of a transfer function between torque ripple and mounting forces. Generic studies of a simplified mounting structure coupled to the machine model are presented here. Acoustic testing of several machine configurations on a production mount has been carried out to investigate 36th order noise in three phase machines and 72nd order noise in six-phase machines. Electromagnetic modeling and dynamic response simulations suggest that the six-phase machine is

*Corresponding author. Tel.: +1-573-341-4670; fax: +1-573-341-4607.
E-mail address: eversman@umr.edu (W. Eversman).

0022-460X/$ - see front matter
doi:10.1016/j.jsv.2004.04.012

inherently quieter. This is supported by experimental results. A test fixture for the measurement of torque ripple has been developed. Experimentation shows that the relative amplitudes of torque ripple in three- and six-phase machines correlates with relative noise levels. In addition, in torque ripple measurements, machine mounting characteristics are substantially altered and a predictably large reduction in radiated noise is realized.

1. Introduction

In some automotive applications noise generation in the electrical energy management system is a competitive issue. For many years the heart of this system has been the three-phase claw pole, or Lundell, alternator. The rotor of a typical claw pole alternator is shown in Fig. 1(a). There are six pole pairs and the field winding is around the shaft axis. Fig. 1(b) shows a 36 slot stator which is typical of conventional three phase machines. This machine produces a high energy density and is relatively inexpensive to manufacture. The usual electromagnetic configuration of this machine favors the generation of noise at 36 times the machine speed (36th order), and at idle speed, particularly when there is a high-energy demand after start up, the resulting noise, typically at around 1000 Hz, can be detectable in the passenger compartment in vehicles in which other noise sources have been reduced. Noise levels of a machine with a given electromagnetic configuration appear to vary from one installation to another in which the mounting lug geometry and the mounting structure providing the interface between the machine and the engine block are the only differences.

In a concurrent study of electromagnetically generated noise in claw pole alternators [1–3], lumped parameter and magnetically equivalent circuit models have been developed which provide simulations of phase currents, phase voltages and torque ripple. It is found that in addition to cogging torque, present even without an electrical load on the machine and related to the field current and the number of slots on the stator, there is additional torque ripple induced by phase current and voltage. In the typical three-phase machine, with six pole pairs on the rotor and 36 slots on the stator, it is found that a strong electromagnetic generating mechanism exists for 36th order (and harmonics) torque ripple. In a six phase, six pole pair, 72 slot machine, cogging torque and phase current and voltage-induced additional torque ripple is present in 72nd order (and

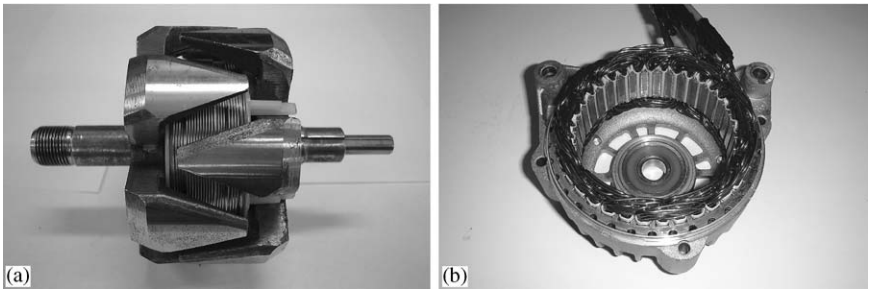

Fig. 1. (a) Claw pole rotor showing six pole pairs and field winding about the rotor axis. (b) Three phase, 36 slot stator. Mounting lugs upper left and right.

harmonics). Refs. [1–3] show that in case of the conventional three phase, 36 slot machine, refinements such as variations of pole geometry, can provide modest benefits in the reduction of torque ripple. Six phase machines, on the other hand, show the potential for large reductions of torque ripple generation, relative to the conventional machine, and this has been verified by experiment as reported here.

In a previous investigation [4] it was assumed that an important noise radiation mechanism in claw pole alternators is dynamic response of the stator , and consequently the housing, to rotating electromagnetic forces between the rotor and stator. This has resulted in detailed FEM models for the generally complex geometry of the stator or stator and housing. Dynamic effects due to rotor rotation and shaft and bearing flexibility were apparently not considered. A complicating factor making it difficult to definitively isolate noise mechanisms is the potential for the 36th order (six times the electrical frequency, as quoted in Ref. [4]) to appear in radial forces on the stator and in the torque ripple. Anecdotal evidence suggests that machines which are water jacketed for cooling show little reduction in radiated noise. Limited experimentation in the present study in which a shroud was placed around the machine showed minimal effect on measured noise. This suggests that there exist noise radiation mechanisms in addition to housing dynamic response to radial forces which are significant. In the investigation reported here, torque ripple, and machine and mounting structure response to it, is studied as an important noise radiation mechanism.

The investigation begins with acoustic and torque ripple measurements obtained for (electrically) loaded machines on a dynamometer in the anechoic facility at the University of Missouri-Rolla. Machines are either shaft driven, or belt driven as in a production installation. Acoustic measurements and mounting structure acceleration measurements were made for machines mounted on a production mount and belt driven. Tests reported here were made on three phase, six pole pair machines, with 36 stator slots, and two claw pole geometries, to assess the potential effect of claw pole geometry on noise. Additional tests were made on a six phase, six pole pair, 72 slot machine, to assess the effect of machine electromagnetic configuration on noise radiation. Acceleration measurements in a direction parallel to the machine axis were made on the production mount to investigate the conversion of torque ripple into mount acceleration for correlation with noise measurements and torque ripple measurements.

A novel fixture for the measurement of torque ripple was constructed in which the machine housing is allowed a degree of freedom in rotation about the machine axis. Rotation is constrained by a leaf spring on which the required constraint force is measured and used as an indirect measure of torque ripple. Torque ripple measurements were made for correlation with noise measurements and axial accelerations for machines mounted on the production mount. In addition, noise measurements on the torque ripple fixture were made for comparison with similar measurements on the production mount. Noise levels on the torque ripple fixture are significantly reduced, suggesting that the mounting geometry is important in noise radiation.

Experimental results suggest that the dynamic response of the machine/mount combination provides an important path for noise radiation. In an ideal mount, the only forces generated should create a couple to react to the rotation of the machine induced by torque ripple. In an actual mount, forces transverse to the axis of this couple are produced, and these can be symptomatic of structural noise radiation mechanisms. In order to determine how torque ripple is converted to mount response, and potential acoustic radiation, a low-order model of the alternator which includes shaft flexibility, gyroscopic effects, shaft bearing stiffness asymmetry,

mounting lug geometry, machine/mount interface stiffness, and mounting structure dynamics has been created. The dynamic model of the machine is coupled to a reduced order FEM model of the mounting structure by component mode synthesis. The coupled model provides a rapid simulation of dynamic response in the form of a transfer function between torque ripple and mount forces. Generic studies of a simplified mounting structure coupled to the lumped parameter machine model are presented here. It is found that coupling of torque ripple into transverse mount forces is related to machine mass asymmetries, the geometry of the mounting lugs and structure, bearing stiffness, gyroscopic effects, compliance in the machine housing rotational degree of freedom, and the mount geometry. It is shown that in addition to electromagnetic source mechanism reduction (torque ripple), six-phase machines have advantages in reduction of the conversion of torque ripple to mount forces.

2. Experimentation to connect torque ripple and noise

To investigate the connection between electromagnetic effects and radiated noise, a series of tests have been carried out to measure noise, mount acceleration, and torque ripple, with special attention to frequencies at the 36th order of machine rev/min for six pole pair, 36 slot, three phase machines, and 72nd order for six pole pair, 72 slot, six phase machines. Noise and mount acceleration testing was carried out for a machine on a standard production mount. Torque ripple testing was carried out on a specially designed torque ripple fixture. This section gives details of these experiments.

2.1. Test facility

The experimental facility was designed for the testing of small motors and generators. It consists of an anechoic chamber, an externally mounted 20 horsepower dynamometer, and a test stand suitable for the simulation of several machine mounting and drive conditions. Data acquisition software and hardware with full spectral and order tracking capabilities is available.

The anechoic room has an interior volume of $8 \times 8 \times 8$ feet. The interior features shallow wedges, which provide the desired acoustic characteristics without excessively thick walls, and thus allows for smaller exterior dimensions. Fittings in the walls of the chamber provide access for power and data acquisition cables. An acoustic tunnel provides access for the dynamometer drive mechanism. The cut-off frequency for anechoic measurements is approximately 300 Hz, adequate for the present investigation. The dynamometer is a 4-quadrant 20 horsepower unit. Although relatively noisy in operation, inside the anechoic chamber the noise from the dynamometer is not of significance for the acoustic tests.

Sound pressure level measurements are made with three microphones on an arc centered 30 cm from the center of the machine in a vertical plane through the machine axis. Microphone locations are at 0 and $\pm 45^{\circ}$ from the vertical. SPL comparisons are consistently reported for a single microphone.

The test stand in the anechoic room has an easily changed geometry which allows mounting of a wide variety of experiments. It features a belt-driven power take off from the dynamometer. Through a pulley and idler arrangement it is possible to drive the test machines directly from a drive shaft or from a belt arrangement similar to a production configuration. Fig. 2 shows a typical experimental setup, with a belt-driven machine on a production mounting structure.

Advantage was taken of the versatility of the test stand to measure torque ripple with the setup depicted in Fig. 3. The alternator with extended shaft is supported on two external bearings, allowing it freedom to rotate about the shaft axis. When the alternator is turned at speeds representative of those in its normal service, and with a current load draw from the alternator, a net torque and an oscillatory torque ripple is generated by the alternator. This torque is indirectly measured as a force variation at the end of a cantilever restraining beam by a force transducer.

Fig. 4 shows some detail of the production mount, revealing potentially efficient acoustic radiation surfaces. The location of the accelerometer on the mount is shown with the axis of measurement parallel to the machine axis.

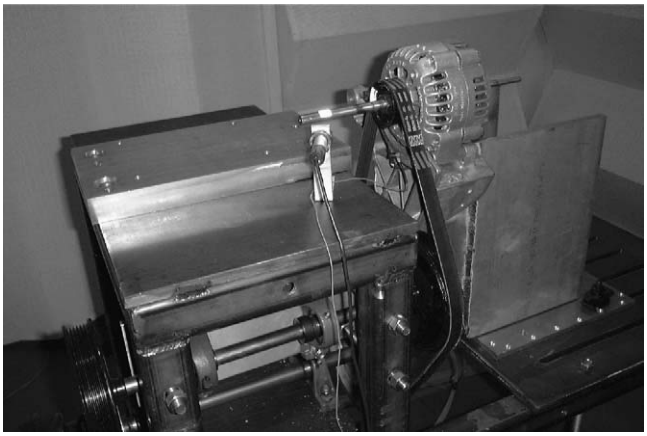

Fig. 2. Acoustic test facility showing a belt-driven alternator on a production mount. Extended shaft is used on the torque ripple test fixture.

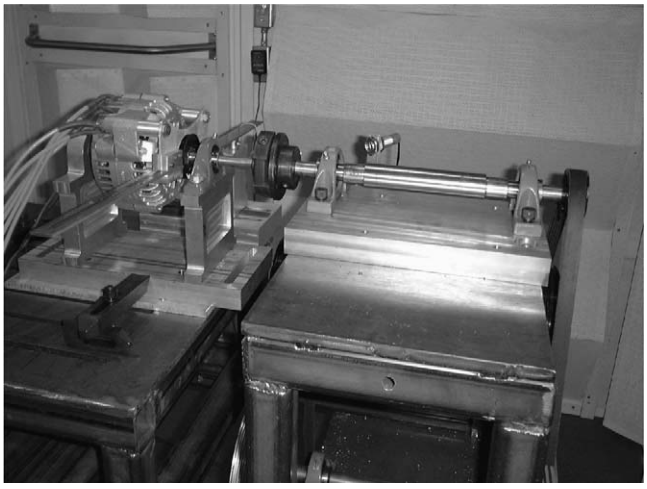

Fig. 3. Test fixture for torque ripple measurement. Extended shaft machine is supported in two additional external bearings. Rotational constraint is provided by a leaf spring restrained by a force transducer.

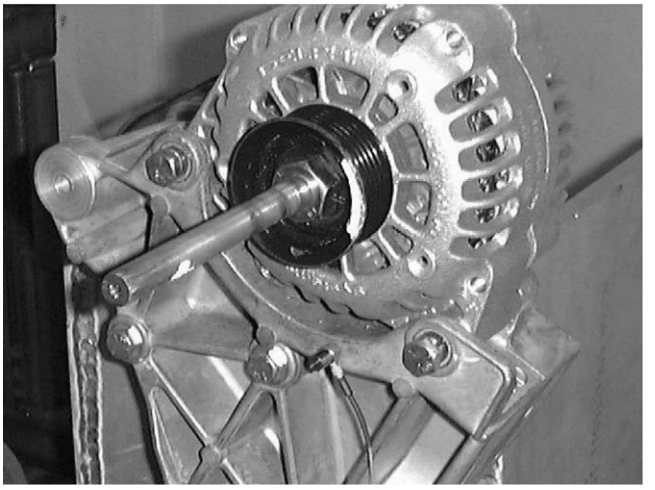

Fig. 4. Detail of production mount and location of accelerometer. Machine has an extended shaft for torque ripple fixture.

2.2. Machine configurations

Tests on three variations of the alternator are reported here. Two versions of a standard three phase, delta connected machine were used. They were apparently identical, except for the details of their rotors. The first of the rotors was cold formed (CF) with a minimum of extra machining, representative of a production machine. This machine features rotor claws with sharp leading and trailing edges. A second version features rotor claws which are slotted in a radial plane. This substantially modifies the electromagnetic field of this alternator in comparison to the standard machine, and is expected to generate artificially high amplitudes of torque ripple and noise. The third configuration tested was a prototype six pole pair, 72 slot, six phase machine connected in wye. The acoustic characteristics of this machine are predicted to be significantly different from the other machines, with less torque ripple and lower noise.

Tests were performed with an electrical load of 5 A at machine speeds in the range 1500–3200 rev/min. This is representative of idle conditions with a high electrical load, a situation where the noise problem tends to be the most significant. Torque ripple tests were not run at the highest machine speeds in this range because of a slight run out in the extended shafts of the machines modified for these investigations.

3. Experimental results

3.1. Production mount acoustic results

Figs. 5(a) and (b) are waterfall plots summarizing the results of the sound level and acceleration measurements for the six pole pair, 36 slot, three phase machine with the CF rotor on the production mount. Both plots confirm the prediction from electromagnetic modeling [1–3] that

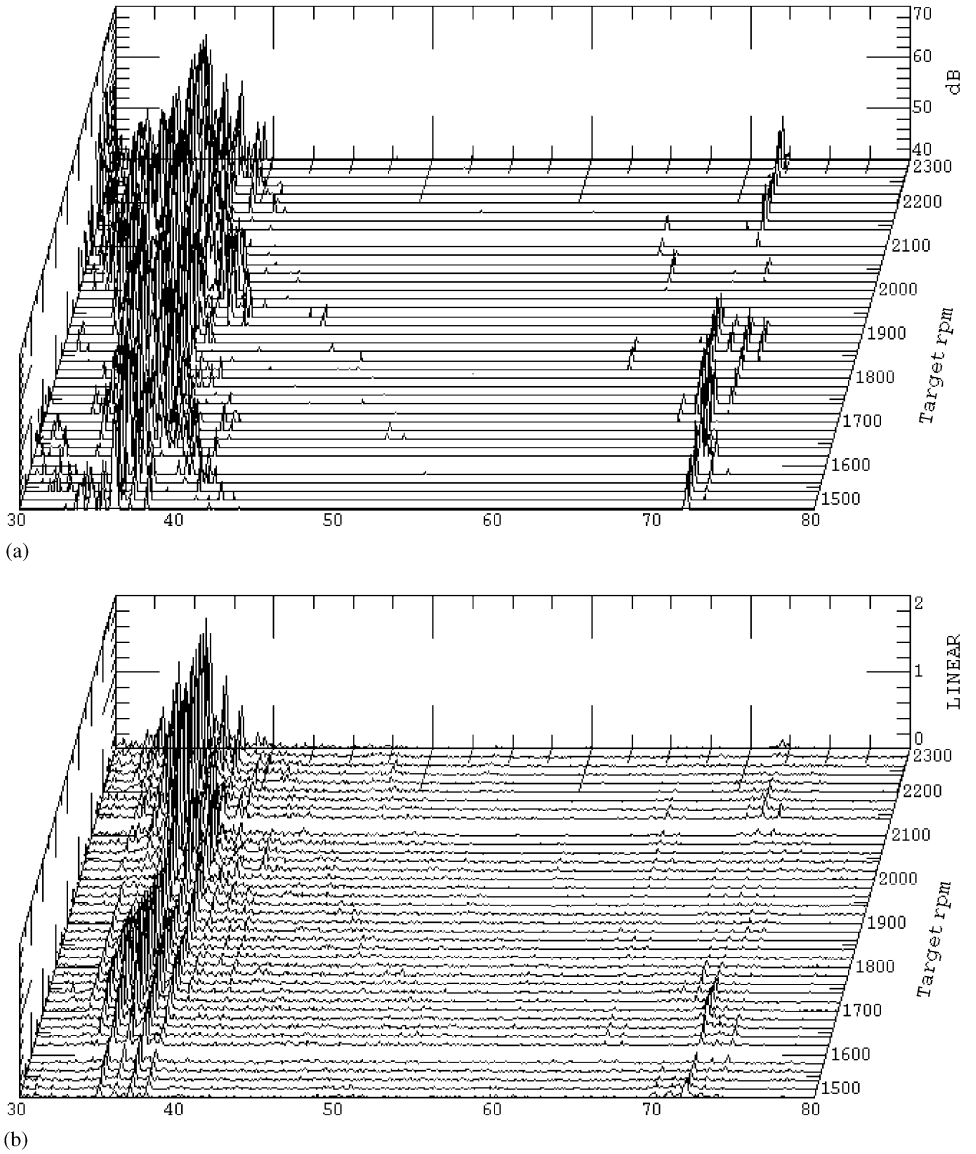

Fig. 5. Waterfall plots for the CF rotor, three phase machine. (a) Sound pressure level; 36th order: 69.5 dB at 2220 rev/min, 72nd order: 52.5 dB at 1640 rev/min. (b) Acceleration amplitude; 36th order: 2.45 at 2140 rev/min, 72nd order: 0.33 at 1680 rev/min.

36th order and harmonics (72nd order for the range shown here) should dominate the torque ripple signature, and therefore the noise and acceleration signatures. Comparison of the plots clearly shows the relationship between the noise level for 36th order, and the corresponding acceleration of the production mount in the direction parallel to the axis of the alternator shaft. In addition, a similar relationship can be seen for 72nd order, with a much lower amplitude. Figs. 6(a) and (b) are the sound level and acceleration measurements for the slotted rotor

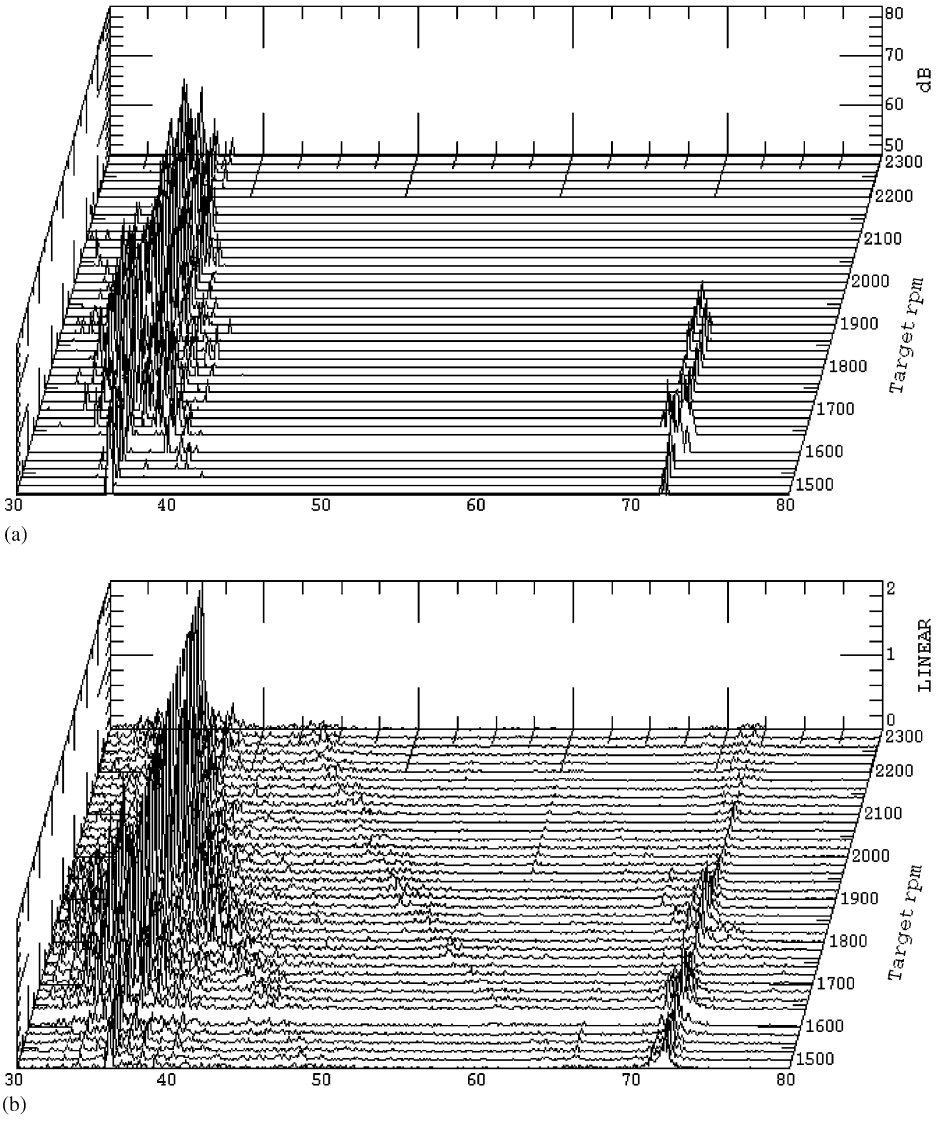

Fig. 6. Waterfall plots for the slotted rotor, three phase machine. (a) Sound pressure level; 36th order: 78.6.12 dB at 2194 rev/min , 72nd order: 63.6 dB at 1915 rev/min. (b) Acceleration amplitude; 36th order: 3.76 at 2194 rev/min, 72nd order: 0.97 at 2194 rev/min.

machine. As with the CF rotor, 36th order and 72nd order dominate both sound and acceleration measurements.

In 36th order, the slotted rotor had the higher maximum noise level (78.6 dB at 2194 rev/min), followed by the CF rotor (69.5 dB at 2220 rev/min). This ranking also holds true for the mount acceleration, with the acceleration of the slotted rotor being 3.76 at 2160 rev/min, and CF acceleration 2.45 at 2140 rev/min. These are maximum sound levels and maximum accelerations in the specified waterfall plot, and are not at exactly the same machine speed. Acceleration

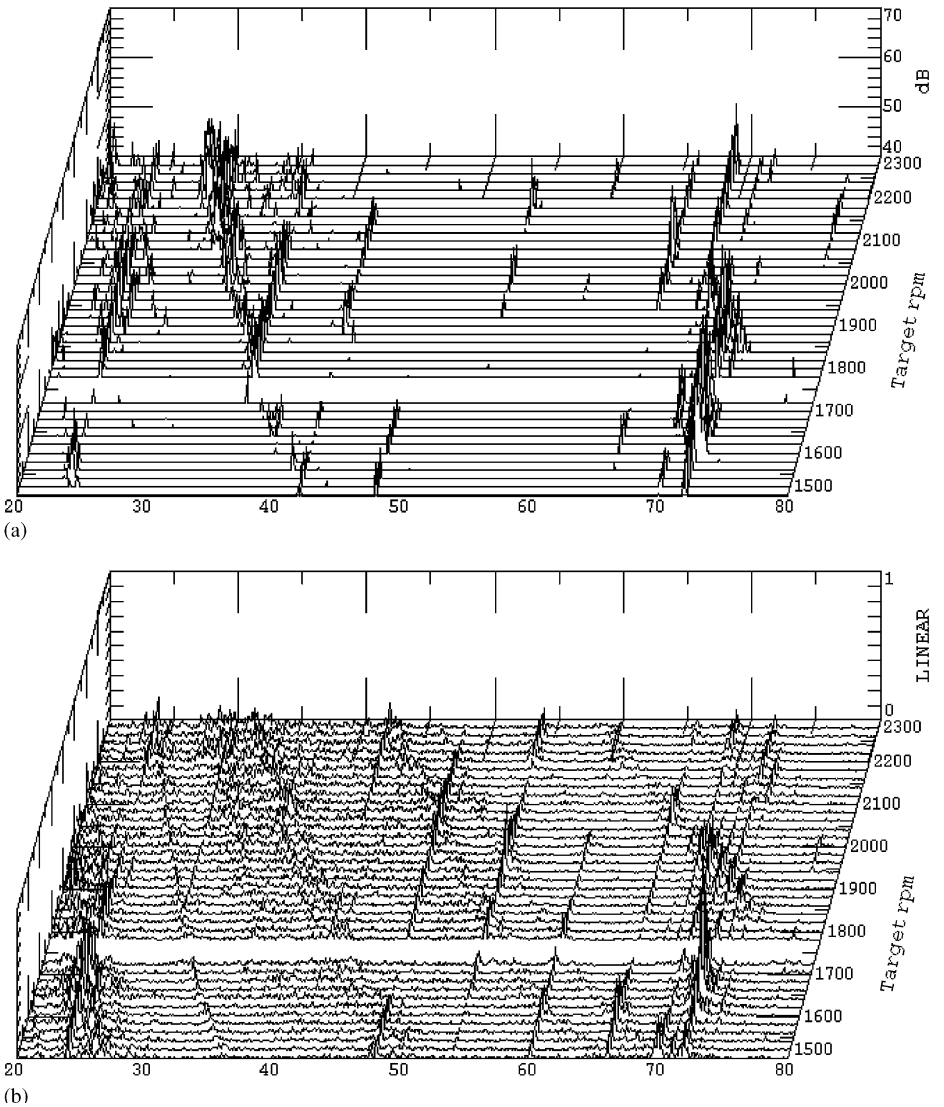

Fig. 7. Waterfall plots for the six-phase machine. (a) Sound pressure level; 24th order: 52.4 dB at 1560, 36th order: 51.6 dB at 1980 rev/min, 72nd order: 62.8 dB at 1660 rev/min. (b) Acceleration amplitude; 24th order: 0.61 at 1660 rev/min, 36th order: 0.17 at 2080 rev/min, 72nd order: 0.93 at 1660 rev/min.

amplitudes quoted are on a linear voltage scale, but were not calibrated to acceleration amplitude units, and are hence useful only for comparison. As predicted, the slotted rotor is a very noisy machine and has the largest axial mount accelerations to match. Machine speeds at which maximum noise occurs and at which maximum acceleration occurs for each machine are not exactly the same, but are relatively close.

This ranking also holds true for 72nd order measurements of noise level and acceleration. For 72nd order, the slotted and CF rotors had measured maximum sound levels of 63.6 and 52.2 dB,

respectively. Measurements of the maximum acceleration for the slotted and CF rotors were 0.97 and 0.33.

Electromagnetic modeling predicts that for a six pole pair, 72 slot, six-phase machine, 72nd order and harmonics should dominate the torque ripple noise signature. It is expected that this will also be true for the noise and acceleration signatures. The six-phase machine displays acoustic characteristics that are significantly different from the three-phase machines tested, as shown in Figs. 7(a) and (b). For this machine 72nd order dominates acoustic data, with a maximum level of 62.8 dB recorded at 1660 rev/min. Fig. 7(b) confirms that mount acceleration amplitudes also dominate in 72nd order, but at a relative amplitude of 0.93, it is low by comparison to amplitudes measured in 36th order for the three-phase machines. 24th and 36th order also play a lesser role in noise radiation at the speeds tested. The maximum sound and acceleration measurements for the 24th and 36th orders were (52.4 dB, 0.61), and (51.6 dB, 0.17), respectively. The six-phase machine was significantly more quiet than both three-phase machines over the speed range tested.

3.2. Torque ripple measurement results

Figs. 8(a) and (b) are the results of the torque ripple amplitude measurement, as well as the noise level generated by the alternator while in the torque ripple setup, for the three phase, CF rotor machine. Similar results for the slotted rotor machine are shown in Figs. 9(a) and (b). Torque ripple is indirectly assessed by measurement of the force required to restrain the machine from rotation. Force amplitudes quoted are on a linear voltage scale, but were not calibrated to force units, and are useful only for comparison. Comparison of the waterfall plots clearly shows the relationship between the noise level, and the corresponding torque ripple for the 36th order. Also, it should be noted that for this test the 72nd order shows little contribution to the overall noise or torque ripple amplitudes.

In the case of torque ripple, the slotted rotor machine clearly exceeds the other machines (note differences in force scales on the figures). Considering only 36th order, the slotted rotor had the higher amplitude of torque ripple (0.028 at 1800 rev/min) compared to the CF rotor (0.012 at 2100 rev/min). Noise measurement maximums on the torque ripple test stand are low by comparison with measurements on the production mount, but are consistent with torque ripple measurements. The maximum levels for the slotted and CF machines are 70.4, 60.3 dB. Reference to Figs. 5–9 show that the rev/min at which the maximum sound levels occur are not the same as the rev/min at which maximum torque ripple occurs. This can be partly rationalized by the different noise radiation characteristics of the production mount and the difference between the response characteristics for measured torque ripple and noise on the torque ripple stand.

The six-phase machine displays apparently inconclusive data, with the relationship between noise and torque ripple not readily apparent. This is shown in Figs. 10(a) and (b). The reason for this is that the amplitude of the measured torque ripple and the noise generated are both very low.

It is interesting to compare noise measurements on the torque ripple stand (Figs. 8(a), 9(a), 10(a)) to previously reported noise measurements made with machines on the production mount (Figs. 5(a), 6(a),7(a)). Production mount ranking was slotted, 78.6 dB (36th order); CF, 69.5 dB (36th order); six phase, 51.6 dB (36th order), 62.8 dB (72nd order). Torque stand mount ranking was slotted 70.4 dB (36th order); CF, 60.3 (36th order); six phase, (low and inconclusive in 36th and 72nd order).

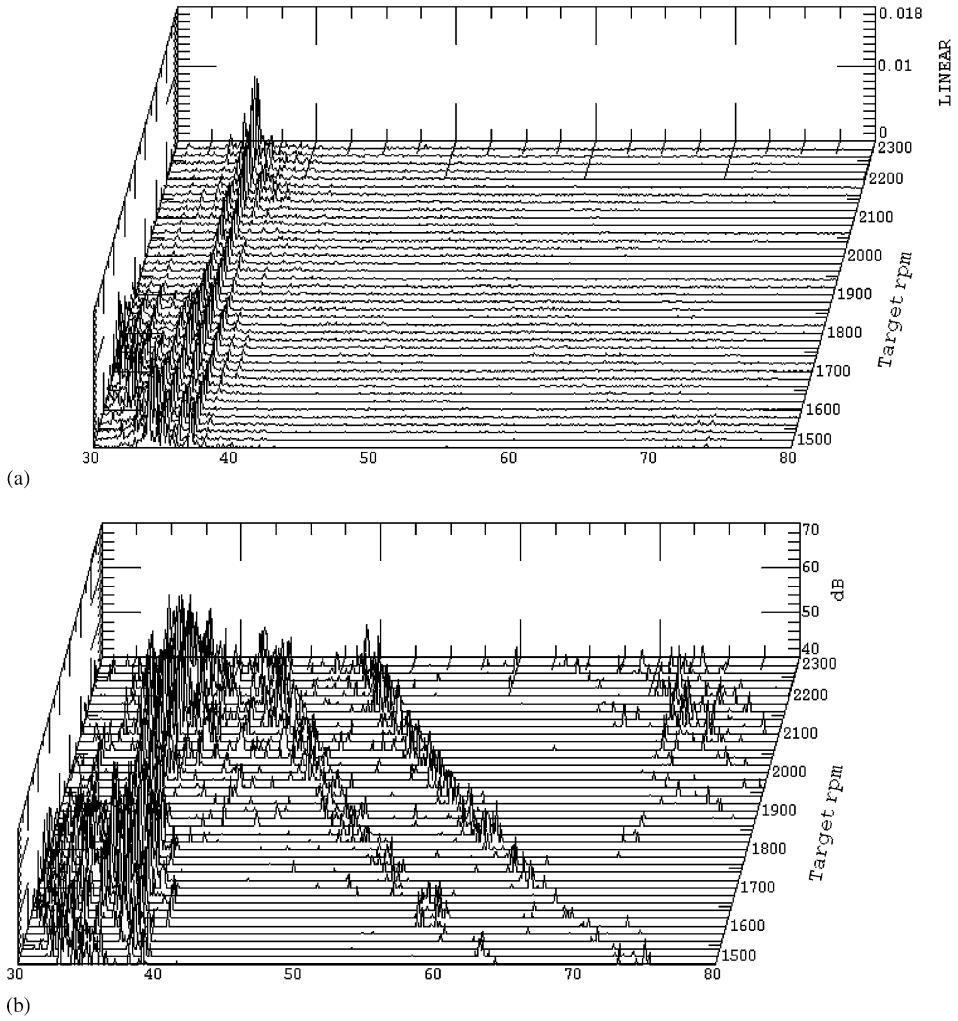

Fig. 8. Waterfall plots for the CF, three-phase machine on torque ripple fixture. (a) Torque ripple; 36th order: 0.012 at 2100 rev/min. (b) Sound pressure level: 60.28 dB at 1600 rev/min.

3.3. Torque ripple and noise

Three features emerge from this data. First, the six-phase machine is substantially quieter than the three phase machines. Electromagnetic modeling [1–3] predicts that torque ripple should be significantly reduced in the six-phase machine, and this is supported by reduced torque ripple and noise measurements. The six-phase machine produces noise predominately in 72nd order, twice the frequency of the corresponding three-phase machines. The transfer function from torque ripple to mount response should provide generally more attenuation, and this will be shown in subsequent modeling of the machine/mount dynamic response. Second, the slotted rotor machine,

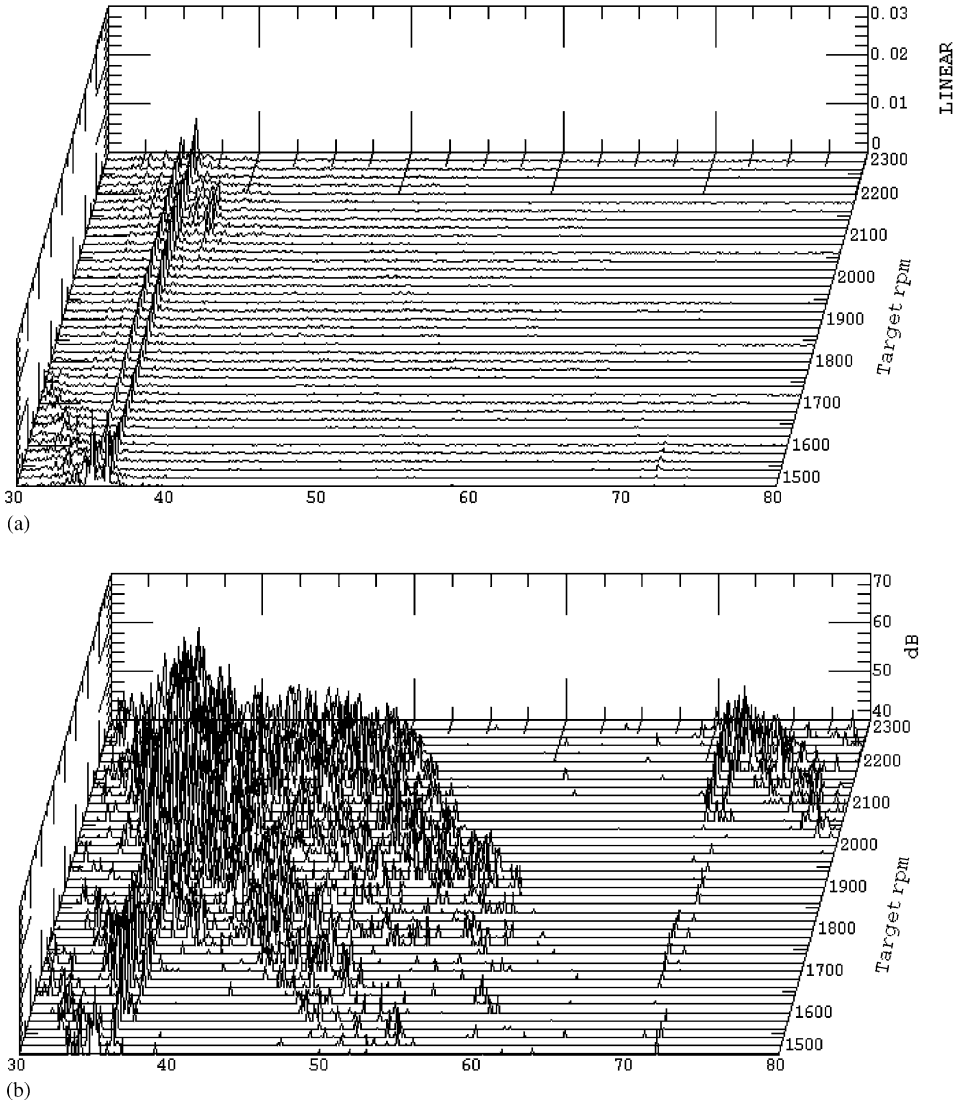

Fig. 9. Waterfall plots for the slotted rotor, three phase machine on torque ripple fixture. (a) Torque ripple; 36th order: 0.028 at 1800 rev/min. (b) Sound pressure level: 70.4 dB at 1720 rev/min.

intentionally configured to produce increased torque ripple, fulfills this expectation in tests, and is clearly the noisier of the two three-phase machines. Finally, the torque ripple fixture is effective in reducing radiated noise. The explanation is rotational compliance introduced by the fixture which decouples the machine from the mount. This behavior can be predicted, as will be shown in a subsequent section dealing with modeling of the machine/mount dynamic response. Evidence supports the conjecture that the coupled dynamics of the machine excited by torque ripple and the mounting structure is a primary noise source. Housing-radiated noise appears to be a secondary source for installations typically encountered for these machines.

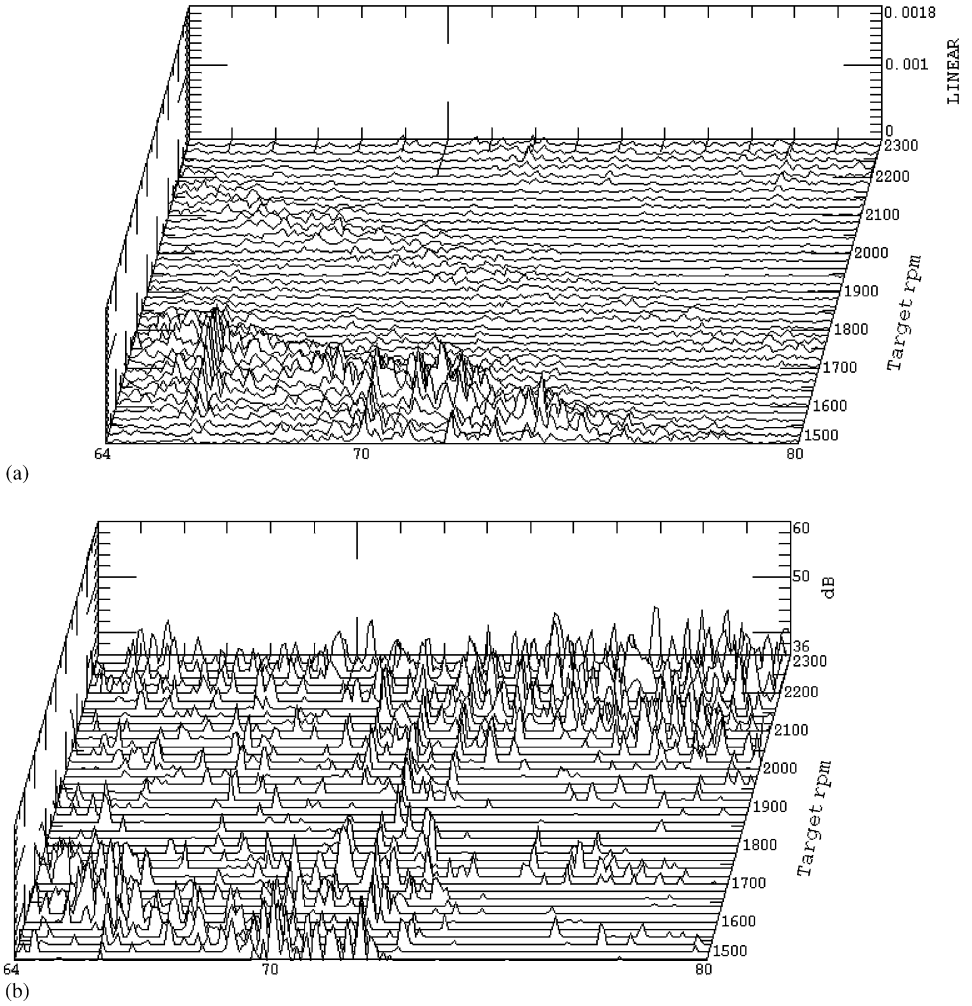

Fig. 10. Waterfall plots for the six-phase machine on torque ripple fixture. (a) Torque ripple; 36th order: 0.0007 at 1600 rev/min. (b) Sound pressure level: below the noise floor.

4. A low-order model for alternator mount dynamics

Experimental evidence shows that there is a relationship between torque ripple and noise in the claw pole alternator at 36th order for the three-phase machine and 72nd order for the six-phase machine. Additional experimental evidence shows that there is dynamic coupling between torque ripple and surface acceleration on the mount in the direction parallel to the torque ripple input axis. Furthermore, it is found that rotational compliance in the mount (a feature of the torque ripple test fixture) leads to substantially reduced noise levels. These results suggest that dynamic response of the machine/mount structure plays a role in noise radiation.

A simplified, low-order model of the machine and mounting structure has been developed to investigate how the rotating machine with torque ripple couples into the mount, and to determine

if this coupling can be reduced or eliminated with proper machine/mount design. With this model it is possible to assess the effect of several machine/mount design features on the transmission of forces into the mount. These features include gyroscopic coupling, shaft stiffness, shaft bearing stiffness, bearing stiffness asymmetry, machine mass distribution, machine mounting lug geometry, machine/mount interface stiffness, belt tension, and mounting structure dynamics.

The low-order model is based on the assumption that the machine consists of a rigid housing supporting a flexible shaft and rotor in two dissimilar bearings. Each of two shaft bearings is described in terms of orthogonal stiffness, not necessarily equal in the three directions. The rotor shaft is modeled as a beam with two identical axes of bending in a finite-element approximation. Sufficient resolution is used to obtain a satisfactory approximation of the first symmetric and anti-symmetric modes of the beam. Gyroscopic effects are included in the rotor dynamics.

Fig. 11 illustrates an idealized layout of a cylindrical machine with one of the mounting lugs shown. The actual geometry of the mounting lugs is unique for a particular application. Attachment of the machine to the support structure at each lug is simulated by stiffness elements in translation and rotation. Important design variables are the location of the mounting lugs relative to a machine reference point, and the stiffness at the interface of the lug and the mounting structure, shown in the figure. Compliance between the housing and the mounting lugs allows an additional rotational degree of freedom about the machine axis relative to the lugs. This compliance is not normally present, but it is included in the present model as a possible additional design variable for the introduction of torque ripple isolation. There is sufficient flexibility in definition of the mounting geometry to represent two, three, or four mounting lugs.

The machine reference point B is the origin for location of mounting springs, centers of mass of the housing and rotor, and rotor bearings. It is on the rotor axis. It will normally be assumed that the rotor and housing centers of mass coincide on the rotor axis, with this point being taken as the

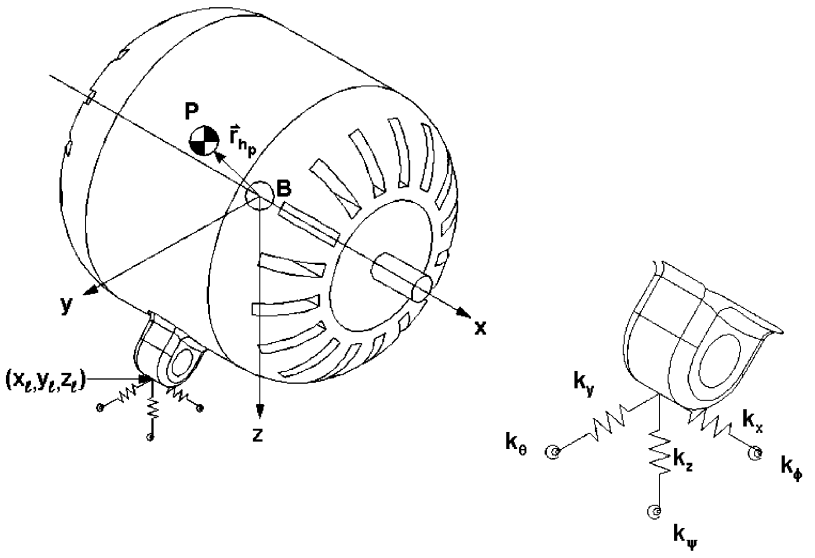

Fig. 11. Idealized geometry of an alternator, emphasizing the generally cylindrical housing and a typical mounting lug, with linear and rotational stiffness.

reference point. Provision is made for the possibility that the reference point and center of mass of the housing and rotor are not coincident. The rotor center of mass is restricted to lie on the axis of rotation, so that the model does not include rotor static unbalance. In addition, the rotor is considered to be axially symmetric with no products of inertia, so that the model does not include rotor dynamic unbalance. Unbalance effects have no contribution at electromagnetic forcing frequencies.

The reference axis system x, y, z has the x-axis forward (toward the drive end), the z-axis down, and the x, y plane in a convenient orientation. Mounting lugs are located by their position relative to the machine reference point B. Bearing locations are also located relative to reference point B.

4.1. Machine/mount interface kinematics and stiffness

Machine mounting lugs are located by coordinates x_1, y_1, z_1, as shown in Fig. 11. Shown also are three linear stiffness elements and three rotational stiffness elements associated with displacements and rotations of the lug relative to the mounting point. Translation spring stiffness coefficients at each mounting point. Rotational spring stiffness coefficients at each mounting point are $k_{\psi_i}, k_{\theta_i}, k_{\phi_i}$. Deflection at the typical lug is defined by three displacements and three rotations $\mathbf{x}_s^{\mathrm{T}} = [x_s\ y_s\ z_s\ \psi_s\ \theta_s\ \phi_s]$. With the assumption of small displacements and rotations, components are determined from three deflections x_b, y_b, z_b of the origin of the axis system, B, and three housing rigid body rotations ψ_b, θ_b, ϕ_b about the axes z, y, x.

Lugs on the mounting structure match machine lugs, as shown in Fig. 12. The displacements and rotations at a typical mounting structure lug (in the same sense as at the matching lug on the machine) are defined by $\mathbf{x}_{\mathrm{sm}}^{\mathrm{T}} = [x_{\mathrm{sm}}\ y_{\mathrm{sm}}\ z_{\mathrm{sm}}\ \psi_{\mathrm{sm}}\ \theta_{\mathrm{sm}}\ \phi_{\mathrm{sm}}]$. These are determined by the structural model of the mounting structure.

Potential energy is synthesized from the potential energy of the individual stiffness elements determined by the relative displacements between the machine and structure mounting lugs. Potential energy associated with the machine/mount structure interface at a typical lug is

$$\mathrm{U} = \tfrac{1}{2}\tilde{\mathbf{x}}_b^{\mathrm{T}}[\hat{K}]\tilde{\mathbf{x}}_b, \tag{1}$$

where $\tilde{\mathbf{x}}_b^{\mathrm{T}} = [x_b\ y_b\ z_b\ \psi_b\ \theta_b\ \phi_b\ x_{\mathrm{sm}}\ y_{\mathrm{sm}}\ z_{\mathrm{sm}}\ \psi_{\mathrm{sm}}\ \theta_{\mathrm{sm}}\ \phi_{\mathrm{sm}}]$.

Each lug will have a different $\tilde{\mathbf{x}}_b$ because deflections in $\mathbf{x}_{\mathrm{sm}}$ are different for each lug on the mount. The total potential energy attributed to all mounting points and corresponding springs is the sum of the contributions of each individual mounting lug and is based on the assembled stiffness matrix $[K_1]$. In general, the assembled stiffness matrix will not be diagonal. This corresponds to static coordinate coupling.

In the case when the mounting structure to which the machine is coupled is very stiff, as, for example, when the machine is mounted directly to the engine block, it is possible to draw conclusions about optimum mounting lug configurations to minimize coordinate coupling. It is found that to minimize machine/mount interface coordinate coupling (the tendency to transform torque ripple input to undesirable mount forces or deflections), the machine center of mass should be at the area centroid of a planar mounting footprint (a line in the case of a two lug system), with the restriction that x mounting spring stiffnesses are equal, the y mounting spring stiffnesses are equal, and the z mounting spring stiffnesses are equal. There is probably little chance that mounting stiffness can be made entirely predictable, principally due to the complexities

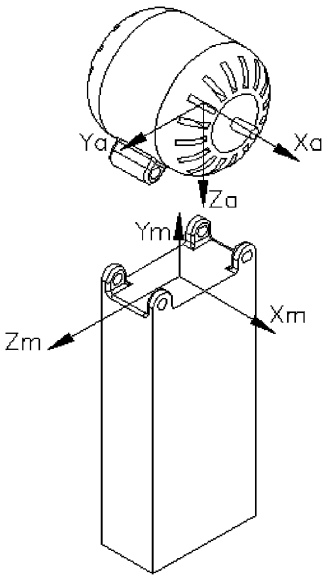

Fig. 12. Coupling of the alternator with a mounting structure, in this case with four lugs on the structure.

introduced by mounting details (e.g. nut/bolt torque, etc.). Simulations must be undertaken which provide for the possibility of poorly defined mount stiffness. Optimum mounting configurations are often not practical due to installation limitations, and the introduction of a relatively flexible mounting structure between the machine and ground (e.g. engine block) defeats to some extent the advantages of an optimum lug configuration.

4.2. Housing dynamics

The housing center of mass P is located relative to the reference point B by the vector $\vec{r}_{H_p} = x_{H_p}\vec{e}_{B_x} + y_{H_p}\vec{e}_{B_y} + z_{H_p}\vec{e}_{B_z}$ (Fig. 11) with components in the reference axis system with origin at B. The angular velocity of this axis system is $\vec{\omega}_B = \dot{\phi}_b\vec{e}_{B_x} + \dot{\theta}_b\vec{e}_{B_y} + \dot{\psi}_b\vec{e}_{B_z}$; ψ, θ, ϕ are Euler angle rotations about z, y, x, assumed infinitesimal. The housing is considered to be rigid so that the velocity of the point P is

$$\vec{V}_p = \dot{x}_b\vec{e}_{B_x} + \dot{y}_b\vec{e}_{B_y} + \dot{z}_b\vec{e}_{B_z} + \vec{\omega}_b \times \vec{r}_{H_p}. \tag{2}$$

The housing is allowed to have an additional angular degree of freedom in rotation about the x-axis, relative to the mounting lugs, denoted by α. This angular rotation is included to model a compliant mounting, intended to explore isolation of torque ripple. Kinetic energy of the housing is

$$T = \tfrac{1}{2}M_H(\vec{V}_p \cdot \vec{V}_p) + \tfrac{1}{2}I_{xx_H}(\dot{\phi}_b + \dot{\alpha})^2 + I_{yy_H}\dot{\theta}_b^2 + I_{zz_H}\dot{\psi}_b^2 \tag{3}$$

and is in terms of degrees of freedom $\dot{x}_b$, $\dot{y}_b$, $\dot{z}_b$, $\dot{\psi}_b$, $\dot{\theta}_b$, $\dot{\phi}_b$, $\dot{\alpha}$. The associated mass matrix is designated $[M_1]$. Mass coupling occurs if the center of mass does not coincide with B and $\vec{r}_{H_p} \neq 0$.

An additional potential energy is associated with the rotational freedom of the housing relative to the lugs. The element stiffness matrix $[K_2]$ is 1×1 with a single stiffness influence coefficient k_α.

4.3. The mounting structure

In order to include the effect of a mounting structure between the machine and ground, additional "element" stiffness and mass matrices must be introduced in a coordinate system which is compatible with the one used to model the machine. The machine housing degrees of freedom are absolute deflections and rotations. The mounting structure therefore also should be modeled so that at least at the interface, the mass and stiffness matrices are in terms of absolute deflections and rotations.

Fig. 12 shows an idealization of a mounting structure as a beam cantilevered at its base. The beam is particularly simple, but all that is required is that an FEM dynamic model of the mounting structure is available. It is expected that the mounting structure be appropriately fixed where "ground" is assumed, and initially free at the mounting lugs. This is referred to as the unconstrained structure. The mounting lugs are taken as constraint points and their deflections are constraint degrees of freedom. In the beam example the constraint degrees of freedom are defined kinematically by the bending deflections and rotations at the end of the beam, so there would be only six constraint degrees of freedom. In general for a mounting structure with four lugs free to move independently, there could be 24 constraint degrees of freedom, assuming that there are three translations and three rotations at each lug.

The approach used to generate a low-order model for the mounting structure is component mode synthesis using constraint modes and constraint-fixed normal modes [5,6]. Briefly, the procedure begins with an eigenproblem for the constraint-fixed structure (constraint degrees of freedom fixed). This generates constraint-fixed normal modes. To extend the basis to include motions at the lugs, constraint modes are computed from a static analysis in which each constraint degree of freedom is assigned a unit value with the remaining constraint degrees of freedom fixed. The extended basis is then constructed from the constraint modes and a suitably truncated set of constraint fixed normal modes. Kinetic energy and potential energy are obtained by an eigenvector expansion in terms of this basis, introducing mounting structure mass and stiffness matrices $[M_M]$ and $[K_M]$. Deflections and rotations at the lugs, defined at the typical lug by the vector of displacements $\mathbf{x}_{\mathrm{sm}}^{\mathrm{T}} = [x_{\mathrm{sm}}\ y_{\mathrm{sm}}\ z_{\mathrm{sm}}\ \psi_{\mathrm{sm}}\ \theta_{\mathrm{sm}}\ \phi_{\mathrm{sm}}]$, are coincident with the amplitudes of the constraint modes. These degrees of freedom already appear in the stiffness matrix for the machine–mount interface, Eq. (1), and this allows a direct assembly procedure for coupling the mounting structure model to the machine model.

The size of the low-order model for the mount is dependent on the structural details of the mount. In the general case described above, 24 degrees of freedom would be associated with the constraint degrees of freedom. The number of constraint fixed normal modes depends on how the constraint fixed natural frequencies compared with the expected range of the driving frequency. In calculations described later, the mounting structure is simplified as a beam (Fig. 12), and six constraint modes and six constraint fixed normal modes are retained, for a total of 12 degrees of freedom for the mounting structure model.

4.4. Shaft dynamics

Rotor and shaft dynamics will be covered in more detail, as the approach here is somewhat unique. Fig. 13 is a sketch of a rotor on a flexible shaft of length L carried by two bearings which are assumed to prevent bending slope of the shaft at the bearing. Shaft displacement at the bearing is elastically restrained by three orthogonal springs $k_{b_x}, k_{b_y}, k_{b_z}$ at each bearing, associated with the coordinate directions shown in the figure.

The rotor kinematics are based on a coordinate system shown in Figs. 13 and 14. This system is oriented with the bearing axis and carried by the rigid housing. Rotor and shaft displacements and rotations are relative to the housing. Displacements are in terms of x, y, z components with x along the rotor axis and y, z normal to the rotor axis. Fig. 14 shows how the orientation of the rotor is described by Euler angles ψ, θ, ϕ; ψ, θ are yaw and pitch angles and ϕ is the rotor rotation angle. The angles ψ, θ are assumed to be small and the rotation angle ϕ is associated with a constant rotation rate Ω so that $\phi = \Omega t$. Shaft stiffness characteristics for transverse motion are approximated by standard FEM techniques. The stiffness matrix is derived using a simple two-element beam model. Bending displacements in two orthogonal directions (y, z) and corresponding bending rotations at three nodes result in an unconstrained 12×12 stiffness matrix. The unconstrained stiffness matrix is reduced to eliminate bending slope rotations at the two ends resulting in an 8×8 shaft stiffness matrix. The rotor is located at the interior node of the assembled shaft.

The constrained shaft stiffness matrix, $[K_3]$, has global degrees of freedom y_1, z_1, y_2, z_2, y_3, z_3, ψ_2, θ_2. Subscript "1" denotes the node (bearing) at the left and subscript "2" denotes the right node (bearing). y_2, z_2 at the interior node provide the transverse deflection of the rotor and are subsequently simply identified as y, z. ψ_2, θ_2 correspond to the bending slopes of the beam at the interior node and define the precession angles for the rotor. They are henceforth identified as ψ, θ. The shaft is assumed rigid axially so three nodal deflections are defined by x. There is a single axial stiffness, the sum of the two bearing stiffnesses, with x. An additional 5×5 diagonal

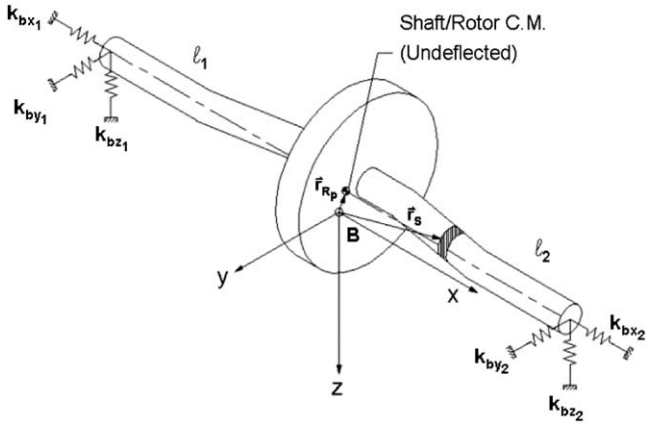

Fig. 13. Geometry of the shaft and rotor showing orthogonal bearing stiffnesses, deflected shaft, and axi-symmetric rotor.

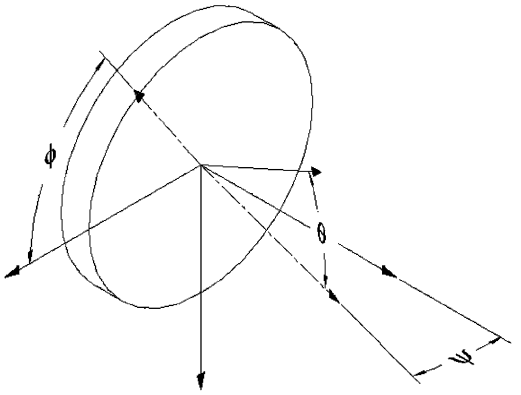

Fig. 14. Euler angles used to describe the orientation of the rotor.

stiffness matrix, $[K_4]$, associated with the bearing stiffness coefficients is in terms of local degrees of freedom y_1, z_1, x, y_3, z_3.

Synthesis of the shaft mass matrix is more complicated due to motion of the housing. It starts with kinetic energy in bending

$$T = \frac{1}{2}\int_L m\vec{V}_s \cdot \vec{V}_s \,\mathrm{d}\zeta, \tag{4}$$

where m is the beam mass per unit length, and L is the shaft length. The shaft is assumed uniform, so that m is constant. $\vec{V}_s$ is the absolute velocity of an element of the beam given by

$$\vec{V}_s = \dot{x}_b\vec{e}_{B_x} + \dot{y}_b\vec{e}_{B_y} + \dot{z}_b\vec{e}_{B_z} + \dot{x}_s\vec{e}_{B_x} + \dot{y}_s\vec{e}_{B_y} + \dot{z}_s\vec{e}_{B_z} + \vec{\omega}_b \times \vec{r}_s, \tag{5}$$

where $\vec{r}_s = x_s\vec{e}_{B_x} + y_s\vec{e}_{B_y} + z_s\vec{e}_{B_z}$ is the position of an element of the shaft relative to the reference axis system B fixed to the housing , as shown in Fig. 13. Components are given by

$$x_s = x_{R_p} + \zeta + x, \quad y_s = y_{R_p} + y(\zeta), \quad z_s = z_{R_p} + z(\zeta). \tag{6}$$

The vector $\vec{r}_{R_p} = x_{R_p}\vec{e}_{B_x} + y_{R_p}\vec{e}_{B_y} + z_{R_p}\vec{e}_{B_z}$ locates the undeflected shaft center of mass. ζ locates a shaft mass element along the shaft. $x, y(\zeta), z(\zeta)$, assumed small perturbations, are shaft motions along and transverse to the shaft relative to the static shaft configuration. The kinetic energy, linearized to neglect terms such as $\dot{\theta}_b z(\zeta), \dot{\psi}_b y(\zeta)$, etc., in the velocities, is then

$$\begin{aligned}\frac{1}{2}\int_L m\vec{V}_s \cdot \vec{V}_s \,\mathrm{d}\zeta = \frac{1}{2}\int_L m\{&[\dot{x}_b + \dot{x} + \dot{\theta}_b z_{R_p} - \dot{\psi}_b y_{R_p}]^2 + [\dot{y}_b + \dot{\psi}_b x_{R_p} - \dot{\phi}_b z_{R_p}]^2 \\ &+ 2[\dot{y}(\zeta) + \dot{\psi}_b\zeta][\dot{y}_b + \dot{\psi}_b x_{R_p} - \dot{\phi}_b z_{R_p}] + [\dot{y}(\zeta) + \dot{\psi}_b\zeta]^2 + [\dot{z}_b + \dot{\phi}_b y_{R_p} - \dot{\theta}_b x_{R_p}]^2 \\ &+ 2[\dot{z}(\zeta) - \dot{\theta}_b\zeta][\dot{z}_b + \dot{\phi}_b y_{R_p} - \dot{\theta}_b x_{R_p}] + [\dot{z}(\zeta) - \dot{\theta}_b\zeta]^2\}\,\mathrm{d}\zeta.\end{aligned} \tag{7}$$

Terms in Eq. (7) are immediately recognizable. The definition of the total mass of the shaft , first mass moment about the center of mass, and moments of inertia are identified as

$$M_s = \int_L m\,\mathrm{d}\zeta, \quad \int_L m\zeta\,\mathrm{d}\zeta = 0, \quad I_{yy_s} = I_{zz_s} = \int_L m\zeta^2\,\mathrm{d}\zeta. \tag{8}$$

With these observations kinetic energy simplifies to

$$\begin{aligned}\frac{1}{2}\int_L m\vec{V}_s\cdot\vec{V}_s\,\mathrm{d}\zeta &= \tfrac{1}{2}M_s[\dot{x}_b+\dot{x}+\dot{\theta}_b z_{R_p}-\dot{\psi}_b y_{R_p}]^2+\tfrac{1}{2}M_s[\dot{y}_b+\dot{\psi}_b x_{R_p}-\dot{\phi}_b z_{R_p}]^2\\ &\quad+\tfrac{1}{2}M_s[\dot{z}_b+\dot{\phi}_b y_{R_p}-\dot{\theta}_b x_{R_p}]^2+\tfrac{1}{2}I_{zz_s}\dot{\psi}_b^2+\tfrac{1}{2}I_{yy_s}\dot{\theta}_b^2\\ &\quad+\frac{1}{2}\int_L m\{2\dot{y}(\zeta)[\dot{y}_b+\dot{\psi}_b x_{R_p}-\dot{\phi}_b z_{R_p}]+[\dot{y}(\zeta)^2+2\dot{\psi}_b\zeta\dot{y}(\zeta)]\\ &\quad+2\dot{z}(\zeta)[\dot{z}_b+\dot{\phi}_b y_{R_p}-\dot{\theta}_b x_{R_p}]+[\dot{z}(\zeta)^2-2\dot{\theta}_b\zeta\dot{z}(\zeta)]\}\,\mathrm{d}\zeta. \end{aligned}\tag{9}$$

Kinetic energy is segregated into three types of contributions. The first contribution is entirely rigid body terms dependent on the shaft mass M_s and shaft centroidal moments of inertia I_{yy_s}, I_{zz_s}. This is denoted by T_R and has associated with it a mass matrix $[M_2]$, which is 7×7 with degrees of freedom $\dot{x}, \dot{x}_b, \dot{y}_b, \dot{z}_b, \dot{\psi}_b, \dot{\theta}_b, \dot{\phi}_b$.

The second type of contribution includes the usual kinetic energy terms for shaft bending,

$$T_S=\frac{1}{2}\int_L m\dot{y}(\zeta)^2\,\mathrm{d}\zeta+\frac{1}{2}\int_L m\dot{z}(\zeta)^2\,\mathrm{d}\zeta. \tag{10}$$

The remaining contributions are the coupling between the housing rigid body motion and the shaft flexural motions,

$$\begin{aligned}T_{RS} &= \frac{1}{2}2\dot{\psi}_b\int_L m\dot{y}(\zeta)\zeta\,\mathrm{d}\zeta+\frac{1}{2}2[\dot{y}_b+x_{R_p}\dot{\psi}_b-z_{R_p}\dot{\phi}_b]\int_L m\dot{y}(\zeta)\,\mathrm{d}\zeta\\ &\quad-\frac{1}{2}2\dot{\theta}_b\int_L m\dot{z}(\zeta)\zeta\,\mathrm{d}\zeta+\frac{1}{2}2[\dot{z}_b+y_{R_p}\dot{\phi}_b-x_{R_p}\dot{\theta}_b]\int_L m\dot{z}(\zeta)\,\mathrm{d}\zeta. \end{aligned}\tag{11}$$

The total kinetic energy associated with the shaft is the sum $T=T_R+T_S+T_{RS}$. Terms of Eqs. (10) and (11) are evaluated by standard FEM procedures. The mass matrices associated with T_S and T_{RS} are evaluated and superposed concurrently to generate a 13×13 mass matrix $[M_3]$ in terms of degrees of freedom $\dot{y}_b, \dot{z}_b, \dot{\psi}_b, \dot{\theta}_b, \dot{\phi}_b, \dot{y}_1, \dot{z}_1, \dot{y}, \dot{z}, \dot{y}_3, \dot{z}_3, \dot{\psi}, \dot{\theta}$. As in the case of the stiffness matrix, bending slopes at the ends of the shaft are constrained. The deflections and rotations at the middle of the shaft, $\dot{y}_2, \dot{z}_2, \dot{\theta}_2, \dot{\psi}_2$ are renamed $\dot{y}, \dot{z}, \dot{\theta}, \dot{\psi}$, the previously defined deflections and precession angles of the rotor. In this approximation shaft kinetic energy associated with rotation of the machine rotor is neglected, and there are no gyroscopic effects due to the rotating shaft.

4.5. Rotor dynamics

For the rotor, gyroscopic effects are essential and are introduced in the following analysis. The rotor center of mass is assumed to lie on the rotor axis of rotation. The rotor center of mass is not necessarily coincident with the reference point B because of a possible shaft offset (suggested in Fig. 13). The rotor is assumed centered on the shaft and at the middle node of the FEM model of the shaft. In general, the rotor center of mass is located in the static configuration relative to B by the vector $\vec{r}_{R_p}=x_{R_p}\vec{e}_{B_x}+y_{R_p}\vec{e}_{B_y}+z_{R_p}\vec{e}_{B_z}$. Consistent with the shaft model the center node has degrees of freedom x, y, z. Additional deflection of the rotor center of mass is therefore $\vec{r}_{R_q}=x\vec{e}_{B_x}+y\vec{e}_{B_y}+z\vec{e}_{B_z}$ with components in the reference axis system. The instantaneous position of

the center of mass of the rotor is therefore $\vec{r}_R = \vec{r}_{R_p} + \vec{r}_{R_q}$, with components in the reference frame B. The center of mass of the rotor has a translation velocity relative to B given by $\mathrm{d}\vec{r}_R/\mathrm{d}t = \dot{x}\vec{e}_{B_x} + \dot{y}\vec{e}_{B_y} + \dot{z}\vec{e}_{B_z}$, where it is noted that $\vec{r}_{R_p}$ is a constant vector relative to the reference axis system B. The angular velocity of the reference axis system B is $\vec{\omega}_b = \dot{\psi}_b\vec{e}_{B_x} + \dot{\theta}_b\vec{e}_{B_x} + \dot{\phi}_b\vec{e}_{B_x}$. The velocity of the rotor center of mass is in linearized form

$$\vec{V}_q = \dot{x}_b\vec{e}_{B_x} + \dot{y}_b\vec{e}_{B_y} + \dot{z}_b\vec{e}_{B_z} + \dot{x}\vec{e}_{B_x} + \dot{y}\vec{e}_{B_y} + \dot{z}\vec{e}_{B_z} + \vec{\omega}_b \times \vec{r}_{R_p}. \tag{12}$$

Linearization resolves linear velocities in the reference frame B (the reference frame B is rotated relative to an inertial frame by the small angles ψ_b, θ_b, ϕ_b) and neglects as higher order the contribution $\vec{\omega}_b \times \vec{r}_{R_q}$.

The kinetic energy of translation of the rotor is

$$T = \tfrac{1}{2}M_H(\vec{V}_q \cdot \vec{V}_q). \tag{13}$$

This gives rise to two element mass matrices. The first is due to translation for the rotor center of mass due to motion of reference frame B (lug motion), and is denoted $[M_4]$. This element mass matrix is of size 6×6 with local coordinates corresponding to global coordinates $\dot{x}_b, \dot{y}_b, \dot{z}_b, \dot{\psi}_b, \dot{\theta}_b, \dot{\phi}_b$.

The second element mass matrix arising from the rotor translational kinetic energy of Eq. (13) is due to coupling of rotor motion with housing motion and rotor motion relative to the housing (frame B). This matrix designated $[M_5]$ is 9×9, with local coordinates corresponding to global coordinates $\dot{x}, \dot{y}, \dot{z}, \dot{x}_b, \dot{y}_b, \dot{z}_b, \dot{\psi}_b, \dot{\theta}_b, \dot{\phi}_b$.

Kinetic energy of the rotor due to rotation about its center of mass involves the angular velocity of the rotor with respect to the reference frame B and the angular velocity of the B frame relative to a fixed frame I:

$$\vec{\omega}_{R/I} = \vec{\omega}_{R/B} + \vec{\omega}_{B/I}. \tag{14}$$

The angular velocity of B with respect to I is (linearized, small angles)

$$\vec{\omega}_{B/I} = \dot{\phi}_b\vec{e}_{B_x} + \dot{\theta}_b\vec{e}_{B_y} + \dot{\psi}_b\vec{e}_{B_z}. \tag{15}$$

The angular velocity of the rotor with respect to the B frame is

$$\vec{\omega}_{R/B} = (\dot{\phi} - \dot{\psi}\sin\theta)\vec{e}_{R_x} + (\dot{\theta}\cos\phi + \dot{\psi}\cos\theta\sin\phi)\vec{e}_{R_y} + (\dot{\psi}\cos\theta\cos\phi - \dot{\theta}\sin\phi)\vec{e}_{R_z}. \tag{16}$$

$\vec{\omega}_{R/B}$ is resolved in the R-axis system fixed on the rotor and rotating with it. When $\vec{\omega}_{B/I}$ is resolved in the R frame, the angular velocity $\vec{\omega}_{R/I}$ components in the rotor fixed reference frame are

$$\begin{aligned}
\omega_{R_x} &= \dot{\phi} - (\dot{\psi} + \dot{\psi}_b)\sin\theta + (\dot{\phi}_b\cos\psi + \dot{\theta}_b\sin\psi)\cos\theta,\\
\omega_{R_y} &= (\dot{\theta} - \dot{\phi}_b\sin\psi + \dot{\theta}_b\cos\psi)\cos\phi\\
&\quad + [\dot{\psi}\cos\theta + (\dot{\phi}_b\cos\psi + \dot{\theta}_b\sin\psi)\sin\theta + \dot{\psi}_b\cos\theta]\sin\phi,\\
\omega_{R_z} &= -(\dot{\theta} - \dot{\phi}_b\sin\psi + \dot{\theta}_b\cos\psi)\sin\phi\\
&\quad + [\dot{\psi}\cos\theta + (\dot{\phi}_b\cos\psi + \dot{\theta}_b\sin\psi)\sin\theta + \dot{\psi}_b\cos\theta]\cos\phi.
\end{aligned} \tag{17}$$

The kinetic energy due to rotation about the center of mass is

$$T = \tfrac{1}{2}I_{xx}\omega_{R_x}^2 + \tfrac{1}{2}I_{yy}\omega_{R_y}^2 + \tfrac{1}{2}I_{yy}\omega_{R_z}^2. \tag{18}$$

In arriving at Eq. (17) it is assumed that the rotor is axially symmetric so that $I_{yy} = I_{zz}$ and products of inertia vanish. It is assumed that the rotor spin angular velocity $\dot{\phi}$ is constant, that is $\dot{\phi} = \Omega$, and Ω is large compared to other angular velocities. With these assumptions the linearized form of the kinetic energy is

$$T = \tfrac{1}{2}I_{xx}[(\Omega + \dot{\phi}_b)^2 - 2\Omega(\dot{\psi} + \dot{\psi}_b)\theta + 2\Omega\dot{\theta}_b\psi] + \tfrac{1}{2}I_{yy}(\dot{\theta} + \dot{\theta}_b)^2 + \tfrac{1}{2}I_{yy}(\dot{\psi} + \dot{\psi}_b)^2. \tag{19}$$

The kinetic energy of Eq. (19) depends on both generalized velocity and generalized displacements. It produces a 5×5 element mass matrix $[M_6]$ in terms of global coordinates $\psi, \theta, \dot{\psi}_b, \dot{\theta}_b, \dot{\phi}_b$, and a 4×4 skew symmetric element gyroscopic matrix $[G_6]$ in terms of global coordinates $\psi, \dot{\theta}, \dot{\psi}_b, \dot{\theta}_b$ which depends on the rotor angular velocity Ω.

4.6. Generalized forces

Generalized forces are derived from virtual work. Torque ripple is characterized by a harmonic moment on the housing acting about the rotor axis of rotation. Virtual work is considered for arbitrary virtual displacements in the global generalized coordinates. There is non-zero virtual work corresponding to only virtual displacements $\delta\phi_b$ and $\delta\alpha$. The corresponding virtual work is $\delta W = M_t\delta\phi_b + M_t\delta\alpha$, from which it is determined that non-zero contributions to generalized force are

$$Q_{\phi_b} = M_t, \quad Q_\alpha = M_t. \tag{20}$$

Torque ripple is assumed harmonic at N_o times the rotor rotational angular velocity Ω, so that

$$M_t = M_{t_0}\mathrm{e}^{\mathrm{j}N_o\Omega t}. \tag{21}$$

N_o is an integer representing the order of shaft angular velocity considered.

4.7. Component assembly

Component mass and stiffness matrices are assembled into global mass and stiffness matrices using standard FEM procedures. Component degrees of freedom are mapped to global degrees of freedom and energies are obtained by superposition of component energies. The size of the model depends on the size of the model of the mounting structure. If the mounting structure is assumed rigid, only 16 degrees of freedom are required. In examples cited here, the mount is modeled as a cantilevered beam, requiring 12 additional degrees of freedom, leading to a total of 28 degrees of freedom in the model. In a case when the mounting structure is of a more general configuration, the number of degrees of freedom would probably not exceed 100.

The assembled system equation is

$$[M]\ddot{\mathbf{q}} + [G]\dot{\mathbf{q}} + [K]\mathbf{q} = \mathbf{Q}_0\mathrm{e}^{\mathrm{j}N_o\Omega t}, \tag{22}$$

where $[M], [G], [K]$ are assembled mass, gyroscopic, and stiffness matrices, $\mathbf{q}$ is the vector of generalized displacements, and $\mathbf{Q}_0$ is the amplitude of the harmonic generalized force vector.

4.8. Modal decomposition

Eq. (22) has no explicit mechanism for dissipation included, and it is difficult to specify quantitatively at this level. As an alternative, a modal decomposition is introduced, based on the normal modes of the non-rotating machine. These normal modes diagonalize the system mass and stiffness matrices and provide a convenient generalized coordinate system with modal amplitudes as the degrees of freedom. Modal damping can then be introduced in each degree of freedom in the form of a diagonal damping matrix. Fraction of critical damping in each mode is assumed the same in the following analysis.

The procedure is to carry out the standard eigenvalue analysis of Eqs. (24), with gyroscopic effects missing. This yields eigenvalues $\omega_i^2,\ i=1,\ldots,N$ (N is the size of the model), and N eigenvectors $\phi_i,\ i=1,\ldots,N$. Eigenvectors are arranged as columns in the modal matrix $[\Phi]$, in ascending order of the corresponding eigenvalue. With the transformation of coordinates $\mathbf{q}=[\Phi]\mathbf{p}$, Eq. (22) is written in terms of modal amplitudes. Diagonal generalized mass and stiffness, and skew symmetric gyroscopic matrices are defined according to

$$[\tilde{M}]=[\Phi]^{\mathrm{T}}[M][\Phi],\quad [\tilde{K}]=[\Phi]^{\mathrm{T}}[K][\Phi],\quad [\tilde{G}]=[\Phi]^{\mathrm{T}}[G][\Phi] \tag{23}$$

with

$$[\tilde{M}][\tilde{\omega}_0^2]=[\tilde{K}], \tag{24}$$

where $[\tilde{\omega}_0^2]$ is a diagonal matrix with the eigenvalues in ascending order. Dissipation is introduced as a diagonal damping matrix of modal damping coefficients, in this case all with the same fraction of critical damping ζ. This yields

$$\ddot{\mathbf{p}}+\{2\zeta[\tilde{\omega}_0]+[\tilde{M}]^{-1}[\tilde{G}]\}\dot{\mathbf{p}}+[\tilde{\omega}_0^2]\mathbf{p}=[\tilde{M}]^{-1}\tilde{\mathbf{Q}}_0 e^{jN_o\Omega t}. \tag{25}$$

Because of the presence of the non-diagonal gyroscopic matrix, Eq. (25) is not entirely uncoupled except when rotor rotation vanishes. Typical range of the fraction of critical damping would be $0.0\leqslant\zeta\leqslant 0.02$.

For steady-state harmonic solution, Eq. (25) is restructured in state variable form:

$$\dot{\mathbf{w}}=[a]\mathbf{w}+[b]\mathbf{u},\quad \mathbf{y}=[c]\mathbf{w}+[d]\mathbf{u},\quad \mathbf{u}=e^{jN_o\Omega t}. \tag{26}$$

The transfer function from input torque ripple to a suitably defined output for a range of rotor speeds Ω (which appears in the gyroscopic matrix as well as in the harmonic generalized force). Useful choices for outputs will not depend on the input $\mathbf{u}$, so that $[d]=[0]$. Desired outputs could be structural accelerations at points on the mounting structure or forces transmitted through the structure. In any case the output matrix $[c]$ is constructed by returning to physical coordinates with postprocessing through the transformation to modal coordinates and the transformation introducing the truncated basis for the reduced order model of the mounting structure. Forces transmitted to ground or forces in stiffness elements at the machine structure interface are obtained using appropriate stiffness matrices.

5. Simulations

It is suspected that a noise radiation mechanism exists which is related to mounting structure response to torque ripple. The mounting structure reacts to loads caused by the response of the machine to electromagnetic torques. An ideal mount would react to machine housing rotation with a couple about the machine axis and no net force. Experimental evidence is that this is not generally the case, and local acceleration on the mount has been observed in the direction of the machine axis (fore and aft), and it is probable that local accelerations in directions normal to the axis of the machine are present. There is therefore coupling of torque ripple into fore and aft, "lateral" (normal to the y machine axis in Fig. 12), and "transverse" (normal to the z machine axis in Fig. 12) . In many mounting structures, fore and aft, lateral, and transverse mount response provide surfaces for efficient acoustic radiation. In addition, net force transmitted to "ground" through the mount (e.g., the engine block), may couple the machine efficiently to a large acoustically radiating structure, for example, an aluminum block.

Simulations have been carried out to examine machine and mount features which induce coupling of torque ripple to mount response or mount forces. The presence of a net force transmitted to "ground" through the mount is considered to suggest a possible noise radiation mechanism. It is found that the location of the machine center of mass relative to the mounting footprint, asymmetry of shaft bearing stiffness, and gyroscopic effects are important in inducing conversion of torque ripple to mount response.

5.1. Rigid mounting structure

It is first assumed that the mounting structure is rigid, in which case the idealized mounting structure in Fig. 12 is "ground". Interesting observations about optimum mounting configurations for the machine can be made with this case. Net forces transmitted at the interface between the machine and rigid mount are used to examine coupling of torque ripple to transverse mount response. For results given here, "rigid" means that the machine is mounted directly to "ground" through the stiffness elements representing attachment fasteners. Essentially the same results are obtained if the mounting structure is very stiff, as shown later.

The configuration studied has four mounting points, each modeled with linear spring restraint in three orthogonal directions as well as corresponding rotational springs. Mounting points are arranged in a rectangular "footprint", as suggested in Fig. 12. Symmetry of the stiffness of the mounting springs is assumed. Machine mass and geometry parameters are roughly those of a production machine. The reference axis system origin is on the rotor axis and centered over the centroid of the rectangular mounting footprint. Geometric parameters to be varied are the vertical location (z_1) of the axis origin above the plane of the mounting footprint and the coordinates of the centers of mass of rotor and housing relative to the axis origin (x_{cm}, y_{cm}, z_{cm}). The center of mass of the rotor and housing are coincident. z_{cm} is taken as zero and the effect of vertical mass offset is entirely accounted for in z_1.

The most favorable configuration places the reference point B at the centroid of the mounting footprint ($x_{cm} = 0, y_{cm} = 0, z_1 = 0$). That is, the center of mass of the machine is at the centroid of the mounting footprint. This is the "optimum", or baseline, configuration. Simulation of this configuration shows that even with asymmetric shaft bearing stiffness, there is no net force

transmitted to "ground" in any direction. There is vertical force (z direction in the machine axis, Fig. 12) at each lug, but the net effect is a couple reacting to machine rotation.

In the usual machine configuration, the plane of the mounting footprint is below the reference axis, placing the mounting lugs below the machine ($z_1 > 0$), as shown in Fig. 4. There is vertical separation between the plane of the mounting footprint and the machine center of mass, providing a coupling of machine rotation into lateral deflection of the machine center of mass. This in turn induces shaft yawing on unsymmetric bearings which is coupled gyroscopically to shaft pitching and thence to machine yawing and pitching and fore and aft motion of the machine center of mass. This is examined in the following three simulations.

First the case with $z_1 > 0$ and symmetric shaft bearings is considered. A net lateral force is found to be introduced into the mount. Then shaft bearings are made unsymmetric, with stiffness from manufacturer's data for the production machine, and with gyroscopic coupling missing. Again, only a net lateral force exists at the mount. Finally, gyroscopic coupling is included, and coupling with fore and aft and transverse mount forces occurs. An additional feature is the possibility of rotational compliance between the machine housing and the machine mounting lugs, introduced in the kinetic energy and potential energy expressions of Eqs. (7) and (8). Four levels of a hypothetical stiffness in this extra degree of freedom, ranging from nearly rigid to relatively compliant are considered in each simulation, identified by the stiffness "kalpha" in units of N m/rad.

Fig. 15 shows 36th order tracks for net force in the machine axis system transmitted to the mount over the machine speed range 1000–4000 rev/min, where noise problems normally exist. The plane of the mounting footprint is representative of a production machine and below the machine center of mass, the shaft bearing stiffnesses are symmetric, and gyroscopic effects are included. Only the net lateral (y-axis) force is shown. Net fore and aft (x-axis) and transverse (z-axis) forces vanish. There is a substantial effect of rotational compliance, and in general this appears as a significant mechanism for reducing the force transmitted to the mount. Fig. 16 is for the case when gyroscopic coupling is neglected and the shaft bearings are made unsymmetric, consistent with manufacturer's data. Net fore and aft and transverse forces again vanish, and the lateral force, shown in Fig. 16, transmitted to the mount is similar in magnitude to the case when the bearings are symmetric and gyroscopic coupling exists. The case shown in Fig. 17 adds gyroscopic coupling to the unsymmetric shaft bearings. There are now net forces transmitted to the mount in all three directions. Fig. 17 (a) shows the lateral force at about the same level as the previous simulations. The new feature is the presence of fore and aft and transverse forces, shown in Figs. 17 (b) and (c). In this machine configuration gyroscopic coupling induces fore and aft and transverse forces. The effect of rotational compliance is again noted in Figs. 16 and 17. The features seen in this simulation are supported by the experimental observation of axial mount acceleration and noise reduction on the torque ripple fixture (rotationally compliant) previously reported.

Other asymmetries in the machine configuration can exist due to center of mass offsets from the reference point B (assumed in the above simulations to be directly above the centroid of the mounting footprint) and mounting spring stiffness variation. These also provide mechanisms for coupling torque ripple to forces introduced into the mount.

The conclusion to be drawn is that machine mounting configuration has a strong influence on forces transmitted to the mount. With the assumption that the mounting structure is rigid, there is

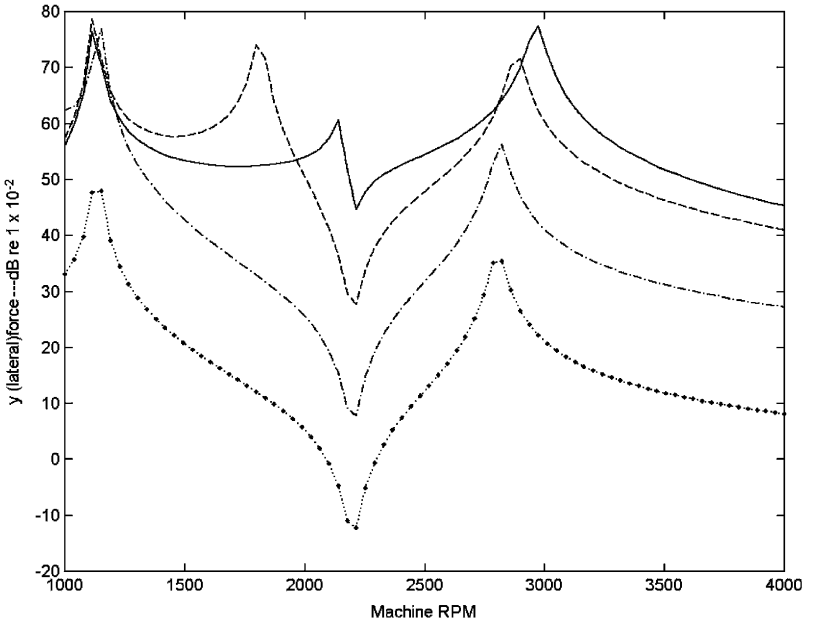

Fig. 15. Net lateral force in 36th order at the mounting lugs for a nominal Lundell machine with ($x_{cm} = 0, y_{cm} = 0, z_1 = 0.04$ m) and a rigid mount. The shaft bearing stiffness is symmetric and gyroscopic effects are included. .. • .. • .., $k_\alpha = 5 \times 10^4$ lb/ft; –·–·–, $k_\alpha = 5 \times 10^5$ lb/ft; — — —, $k_\alpha = 5 \times 10^6$ lb/ft; ————, $k_\alpha = 5 \times 10^7$ lb/ft.

a clearly optimum configuration with the machine center of mass located at the centroid of the mounting footprint. Raising the machine above the mounting footprint introduces net lateral mount forces. The problem is compounded by shaft bearing asymmetry and influenced by (unavoidable) gyroscopic coupling. Additional machine mass asymmetries induce similar coupling effects. There is a strong argument to be made for introducing rotational compliance in the machine design.

5.2. Flexible mounting structure

In the case of a rigid mounting structure it was found that an optimized machine configuration leads to elimination of transverse forces at the machine/mount interface. Here the benefits of optimization are investigated when the mounting structure is flexible. The example model for a flexible mount is a simple beam structure capable of supporting bending in two planes, axial extension, and torsion. There is no structural coupling between bending, extension, and torsion and no "local" characteristics as would appear in the ribbed structure of a production mount as seen in Figs. 2 and 4.

In the simulation given here, the required input includes stiffness and mass data for the beam structure shown in Fig. 15. Coordinate directions here are in the beam axis system. Stiffness is given in terms of EI (for beam bending), GJ (for torsion), and AE (for axial extension). Nominal values used are $EI_x = 8.1 \times 10^4$ Pa m^4 (beam x bending), $EI_z = 3.4 \times 10^5$ Pa m^4 (beam z bending), $GJ = 8.6 \times 10^4$ Pa m^4 (torsion about the beam y axis), and $AE = 3.8 \times 10^8$ Pa m^2, (beam y-axis

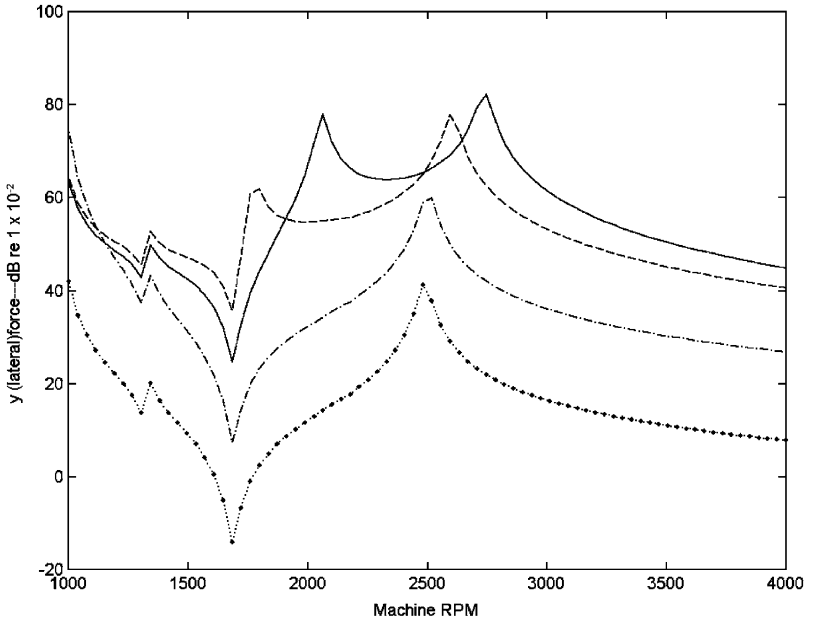

Fig. 16. Net lateral force in 36th order at the mounting lugs for a nominal Lundell machine with ($x_{cm} = 0, y_{cm} = 0, z_1 = 0.04$ m) and a rigid mount. The shaft bearing stiffness is asymmetric and gyroscopic effects are not included. .. • .. • .., $k_\alpha = 5 \times 10^4$ lb/ft; – · – · –, $k_\alpha = 5 \times 10^5$ lb/ft; — — —, $k_\alpha = 5 \times 10^6$ lb/ft; ————, $k_\alpha = 5 \times 10^7$ lb/ft.

extension). Mass properties required are mass per unit length and torsional mass moment of inertia per unit length. Mass per unit length of the beam is $m = 13.9$ kg/m, and the torsional mass moment of inertia per unit length is $i = 4.2 \times 10^{-5}$ kg m^2 /m. The length of the beam model for the mount is 0.25 m. Machine geometry is identical to that used in the simulation of the rigid mount. The first simulation reported will be for a very stiff version of the structure in which all stiffnesses except AE are increased by two orders of magnitude.

The case shown in Fig. 17 is repeated first with the machine mounted on the "very stiff" version of the structure, as noted above. This case has ($x_{cm} = 0, y_{cm} = 0, z_1 = 0.04$ m), with unsymmetric shaft bearing stiffness and gyroscopic effects included. Net forces transmitted to ground at the base of the structure, shown in Figs. 18 (a)–(c), are nearly the same as forces transmitted when the machine is mounted directly to ground, shown in Figs. 17 (a)–(c). This validates the modeling of the mounting structure and also suggests that conclusions drawn about "optimum" machine configurations are appropriate when the mounting structure is stiff.

In the final simulation the nominal (less stiff) structure is coupled to the machine considered in Figs. 17 and 18 with ($x_{cm} = 0, y_{cm} = 0, z_1 = 0.04$), unsymmetric bearings and including gyroscopic effects. General conclusions do not change, as shown in Figs. 19 (a)–(c). It is noted that coupling of torque ripple into mount response leads to moderately increased levels for lateral force and substantially higher levels for fore and aft and transverse forces as compared to the rigid mount and stiff mount cases. This is because dynamic coupling through shaft bearing asymmetry and gyroscopic effects is fed by increased lateral motion of the machine allowed by the flexible structure.

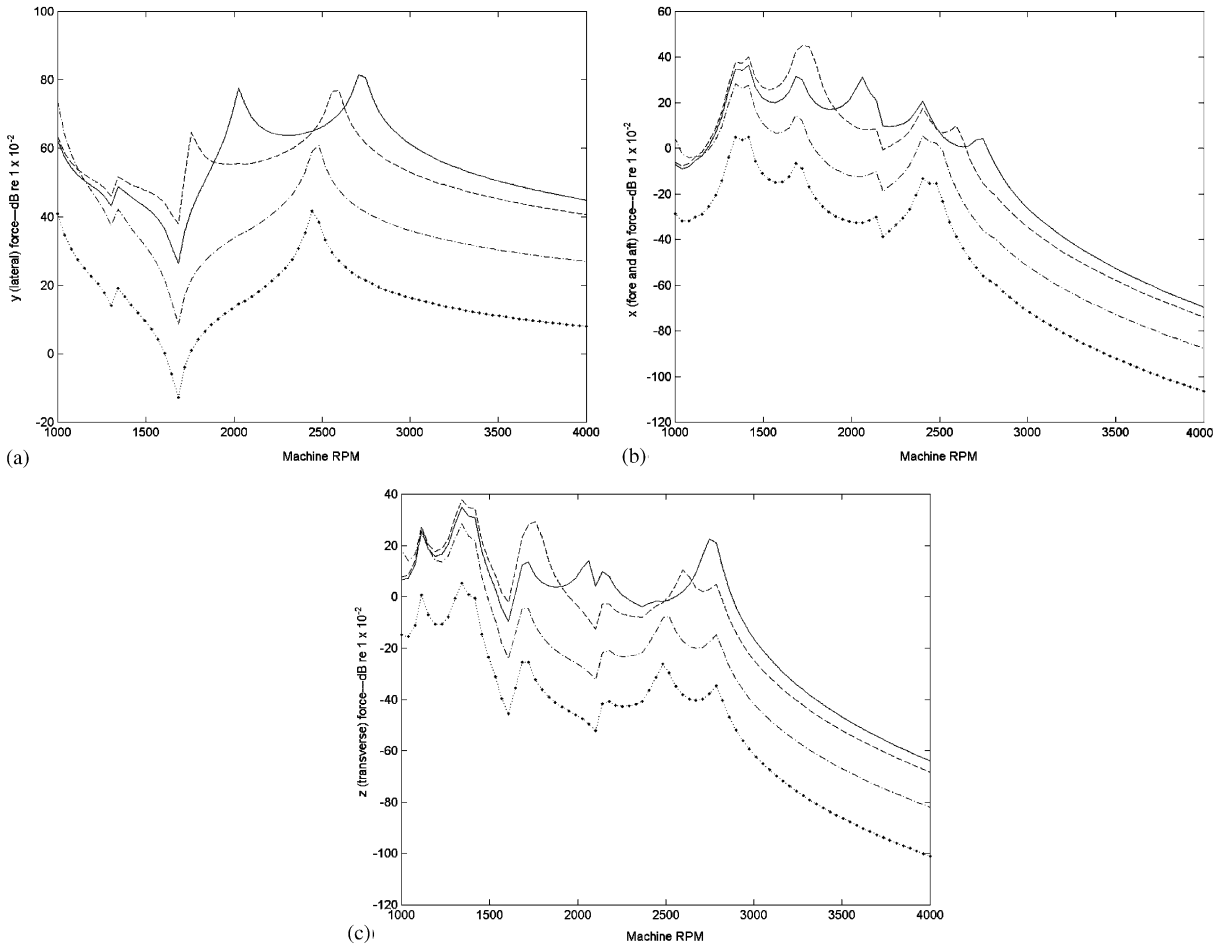

Fig. 17. Net forces in 36th order at the mounting lugs for a nominal Lundell machine with ($x_{cm} = 0, y_{cm} = 0, z_1 = 0.04$ m) and a rigid mount. The shaft bearing stiffness is asymmetric and gyroscopic effects are included. (a) Lateral force (machine y-axis), (b) fore and aft force (machine x-axis), (c) transverse force (machine z-axis). .. • .. • .., $k_\alpha = 5 \times 10^4$ lb/ft; –·–·–, $k_\alpha = 5 \times 10^5$ lb/ft; — — —, $k_\alpha = 5 \times 10^6$ lb/ft; ————, $k_\alpha = 5 \times 10^7$ lb/ft.

Mass asymmetry due to mass offset relative to the centroid of the mounting footprint increases coupling of torque ripple to mount forces. Not specifically simulated here are asymmetry of the stiffness in the coupling between the machine and the mount and structural coupling which may exist in the mount. These static coupling effects also promote coupling of torque ripple into mount response.

6. Six-phase machine

All simulations reported to this point have been for three-phase machines for which the dominant torque ripple is at 36th order of machine rotational speed. Electromagnetic simulations

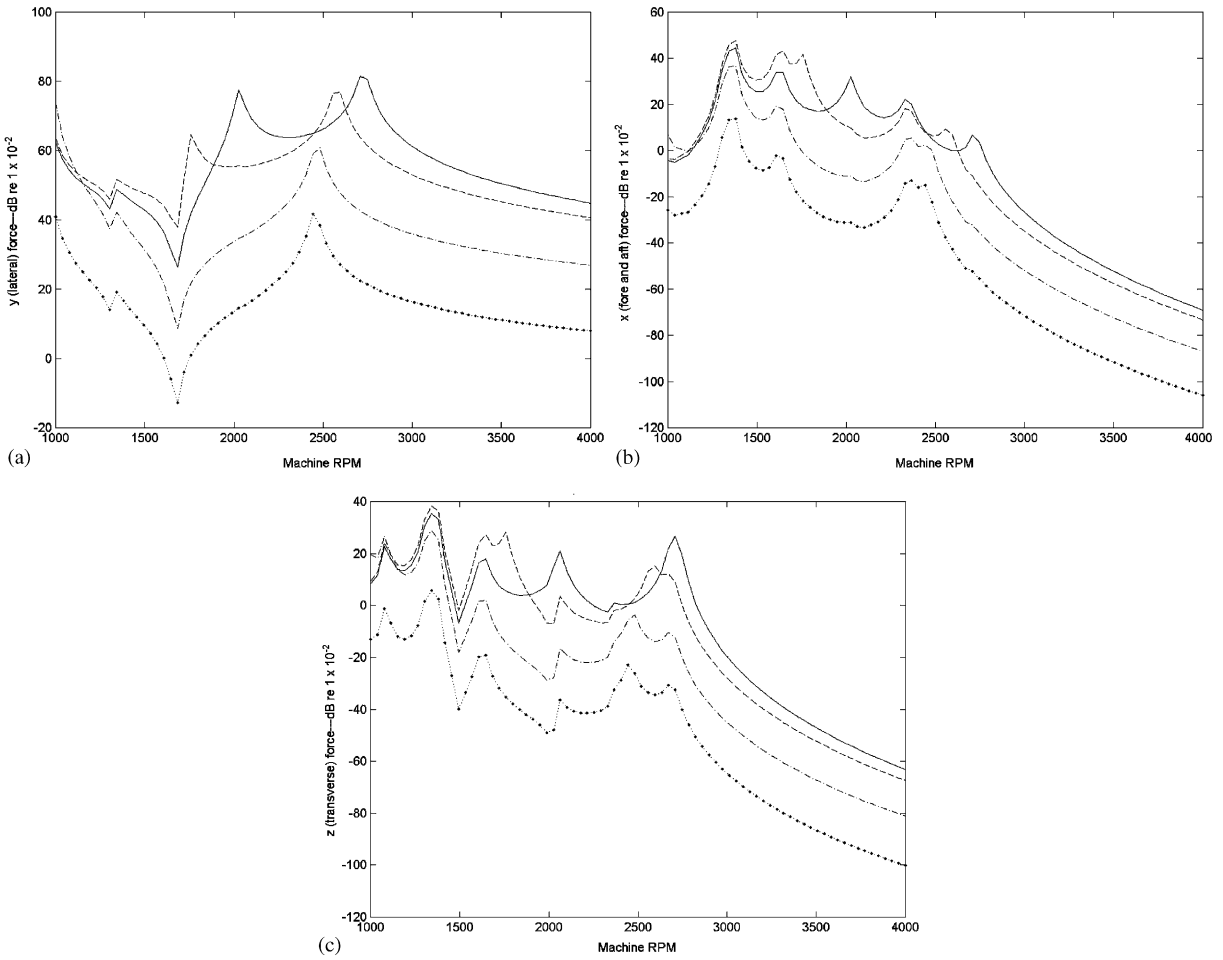

Fig. 18. Net forces in 36th order at the mounting lugs for a nominal Lundell machine with ($x_{cm} = 0, y_{cm} = 0, z_1 = 0.04$ m) and a stiff mount. The shaft bearing stiffness is asymmetric and gyroscopic effects are included. (a) Lateral force (machine y-axis), (b) fore and aft force (machine x-axis), (c) transverse force (machine z-axis). .. ● .. ● .., $k_\alpha = 5 \times 10^4$ lb/ft; –·–·–, $k_\alpha = 5 \times 10^5$ lb/ft; — — —, $k_\alpha = 5 \times 10^6$ lb/ft; ————, $k_\alpha = 5 \times 10^7$ lb/ft.

predict that torque ripple in a six pole pair, 72 slot, six-phase machine should be substantially reduced at 36th order. Torque ripple is predicted to occur at 72nd order, but to be below the amplitude of torque ripple at 36th order in the three-phase machine. Experiments have verified this in noise measurements, acceleration measurements, and torque ripple measurements. In fact, the noise reduction is more than might be accounted for simply on the basis of torque ripple reduction. A simulation of dynamic response of the machine/mount configuration has been carried out with 72nd order torque ripple input but at the same machine operating speed as for the three phase machine (this is the case for the machines considered). The machine and mounting structure considered in Fig. 20 is the test case. Figs. 20 (a)–(c) can be compared directly to Figs. 19 (a)–(c). It is seen that over the speed range of the machine, and in particular in the 1500–4000 rev/min range, forces transmitted to the mounting structure are drastically reduced. The simulations

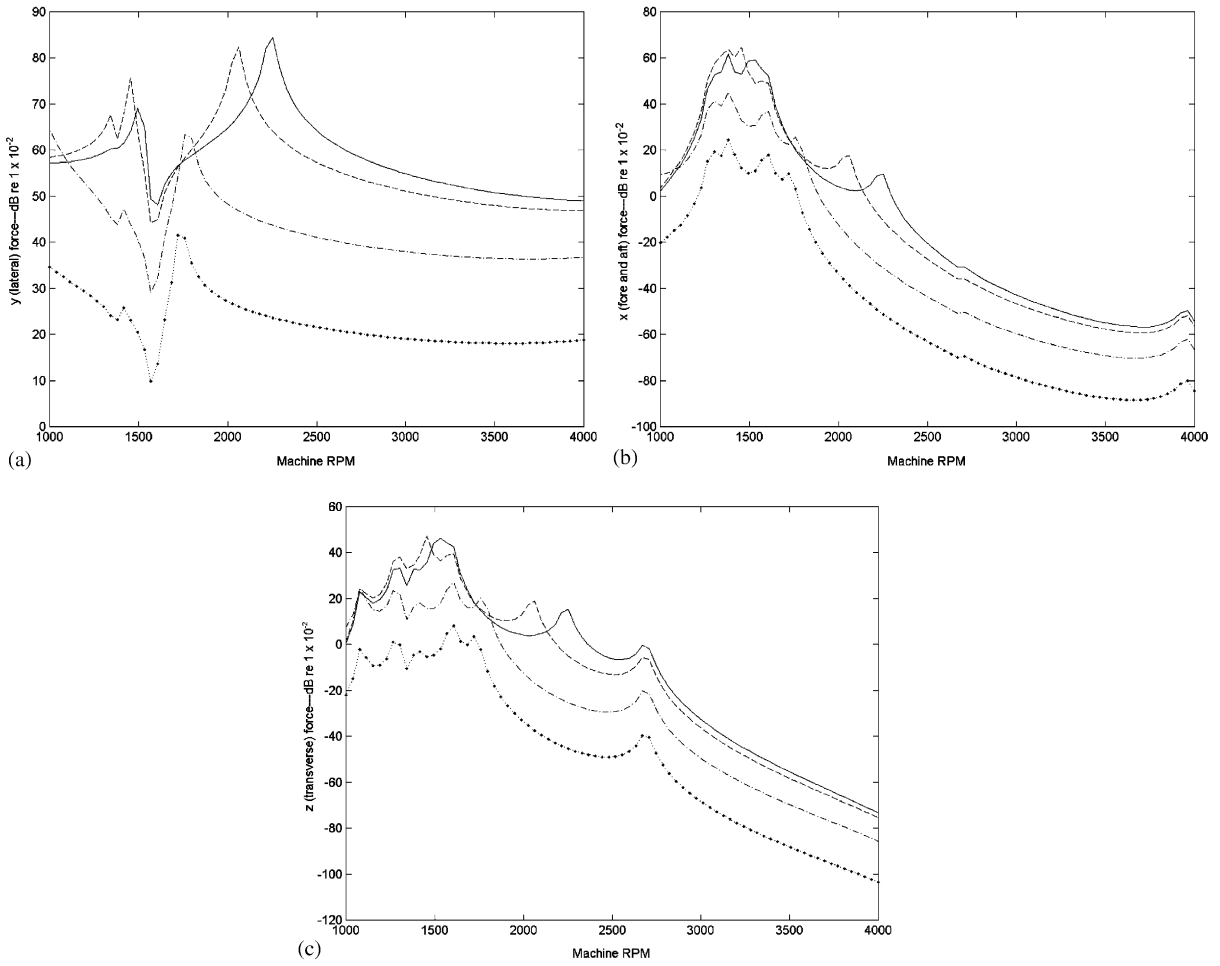

Fig. 19. Net forces in 36th order at the mounting lugs for a nominal Lundell machine with ($x_{cm} = 0, y_{cm} = 0, z_l = 0.04$ m) and a flexible mount. The shaft bearing stiffness is asymmetric and gyroscopic effects are included. (a) Lateral force (machine y-axis), (b) fore and aft force (machine x-axis), (c) transverse force (machine z-axis). .. • .. • .., $k_\alpha = 5 \times 10^4$ lb/ft; –·–·–, $k_\alpha = 5 \times 10^5$ lb/ft; — — —, $k_\alpha = 5 \times 10^6$ lb/ft; ————, $k_\alpha = 5 \times 10^7$ lb/ft.

do not account for the predicted reduction of torque ripple magnitude. The only effect seen is the structural filtering of the higher frequencies associated with the 72nd order torque riple.

7. Conclusion

There are several possible noise radiation mechanisms which may be important in claw pole automotive alternators. Extensive experimentation has led to the conclusion that the conversion of torque ripple into dynamic response of the mounting system contributes to noise at idle conditions under high electrical load. This conclusion is based on several observations:

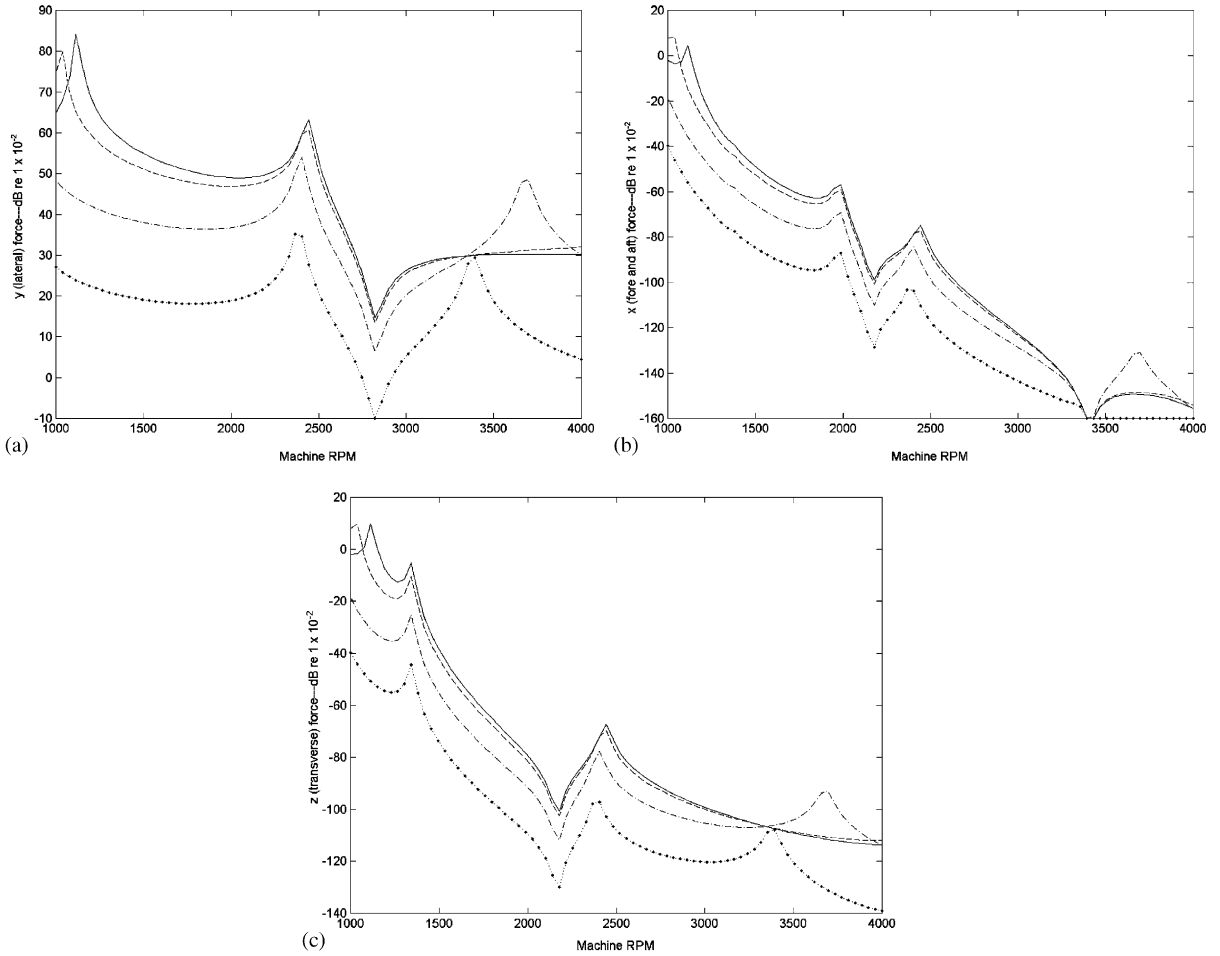

Fig. 20. Net forces in 72nd order at the mounting lugs for a nominal Lundell machine with ($x_{cm} = 0, y_{cm} = 0, z_1 = 0.04$ m) and a flexible mount. The shaft bearing stiffness is asymmetric and gyroscopic effects are included. (a) Lateral force (machine y-axis). (b) fore and aft force (machine x-axis). (c) transverse force (machine z-axis). .. • .. • ..; $k_\alpha = 5 \times 10^4$ lb/ft; –·–·–, $k_\alpha = 5 \times 10^5$ lb/ft; — — —, $k_\alpha = 5 \times 10^6$ lb/ft; ————, $k_\alpha = 5 \times 10^7$ lb/ft.

(1) Measured noise is predominately at 36th order of shaft speed for a six pole pair, 36 slot, three-phase machine. This is consistent with electromagnetic simulations which show that harmonics of the product of phase current and phase voltage at 36th order are the major contributors to torque ripple. Similar conclusions are made for 72nd order torque ripple for six pole pair, 72 slot, six-phase machines.

(2) Torque ripple is predicted to be lower for the six-phase machine. Noise measurements show that the six-phase machine is much quieter than the three-phase machine, more so than predictable simply on the basis of torque ripple. Simulations show that this is to be expected because of structural filtering of higher frequency 72nd order noise characteristic of the six-phase machine.

(3) Acceleration measurements made on the alternator mounting structure correlate well with noise measurements. For the three-phase machine, 36th order is dominant in accelerometer measurements and relative levels of acceleration are consistent with relative noise levels. Similar conclusions apply to 72nd order for the six-phase machine.

(4) Measurements of torque ripple correlate with noise measurements. Higher torque ripple corresponds to higher noise level for both the three- and six-phase machines.

(5) Torque ripple measurements are carried out in a fixture which introduces rotational compliance in the machine mounting. Noise levels measured when machines are running on the torque ripple fixture are substantially lower than when the machine is installed on a production mount. This implicates the mounting structure in the process of noise generation.

(6) Simulations show that coupling of torque ripple into mounting structure dynamic response can occur due to the geometric configuration of the machine, unsymmetric shaft bearing stiffness, and gyroscopic effects. Conversion of torque ripple to mount response also occurs due to mounting stiffness asymmetries, static coupling in the mount, and mass asymmetries of the machine.

(7) Simulations show that with a stiff mounting structure an optimum machine configuration exists which in principle eliminates conversion of torque ripple into net force transmitted into the mount, offering the probability of mount-related noise generation.

(8) Introduction of rotational compliance between the machine housing and mounting structure can have substantial noise reduction benefits. This is deduced on the basis of experiment and simulation.

References

[1] H. Bai, S.D. Pekarek, J. Tichenor, W. Eversman, D.J. Buening, G.R. Holbrook, M.L. Hull, R.J. Krefta, S.J. Shields, Analytical derivation of a coupled-circuit model of a claw-pole alternator with concentrated stator windings, *IEEE Transactions on Energy Conversion* 17 (1) (2002) 32–38.

[2] H. Bai, S. Pekarek, J. Tichenor, W. Eversman, D. Buening, G. Holbrook, M. Hull, R. Krefta, S. Shields, Incorporation of magnetic saturation in a coupled-circuit model of a claw-pole alternator with concentrated stator windings, *IEEE Transactions on Energy Conversion* (2004), to appear.

[3] B. Zhang, H. Bai, S. Pekarek, W. Eversman, R. Krefta, G. Holbrook, Comparison of 3-, 5- and 6- phase machines for automotive charging applications, *Proceedings of the Internatioanl Electric Machines and Drives Conference*, Vol. 3, Madison, WI, June 2003, pp. 1357–1363.

[4] I. Ramesol, T. Bauer, G. Henneberger, Calculation procedure of the sound field caused by magnetic excitations of the claw pole alternator, in: *Proceedings of the Conference on Vibrations and Acoustic Noise of Electric Machinery*, Bethune, France, May 25–26, 1998.

[5] R. R. Craig Jr., *Structural Dynamics*, *An Introduction to Computer Methods*, Wiley, New York, 1981, pp. 467–482.

[6] J.H. Ginsberg, *Mechanical and Structural Vibrations*, *Theory and Applications*, Wiley, New York, 2001, pp. 552–562.